Interaction of a Propeller Slipstream with a Downstream Laminar Boundary Layer

Srivatsav Swaminathan

TU Delft

Interaction of a Propeller Slipstream with a Downstream Laminar Boundary Layer

by

Srivatsav Swaminathan

to obtain the degree of Master of Science in Aerospace Engineering

at the Delft University of Technology

to be defended publicly on Monday, the 15th of December 2025 at 13:30.

Supervisor (s):	Dr. ir. T. Sinnige ir. A. D Sequeira
Thesis Committee:	Prof. dr.ir. L.L.M. Veldhuis Dr. ir. T. Michelis Dr. ir. T. Sinnige ir. A. D Sequeira
Project Duration:	February 2025 - December 2025
Faculty:	Faculty of Aerospace Engineering, TU Delft

TU Delft

Preface

Life can be really unexpected. Around 2 years ago, I was just another student filled with curiosity about aerodynamics. When I applied for the MSc AE programme, I was not entirely confident about being admitted, so I felt really ecstatic when I got into what is one of the best aerospace programmes in the world. My journey here has been quite the roller coaster ride, and I never knew which way the track would go. It all worked out in the end, and while it is tempting to solely attribute this to sheer hard work and resilience, I have also come to believe that sometimes, you just have to go with the flow and trust yourself to persevere no matter what. This is definitely not something a past version of me would have said, but I suppose getting to the end of your Master's degree in Aerospace Engineering, specialising in Aerodynamics, at TU Delft changes your perspective.

This report is a culmination of all the work that I have done during my thesis over the course of the last year. I definitely enjoyed my work during my thesis, and the resources I had access to were simply amazing. As this phase of my learning journey ends here, I would like to express my gratitude to a few people without whom I would have never been able to get to where I am now.

Firstly, I have to thank Tomas Sinnige, my primary supervisor, for allowing me to work on this extremely interesting topic, for helping me frame my study and giving me just the right amount of breadcrumbs to find my way to the answer. Every meeting with him gave me direction and energy and would motivate me to keep working until I reached my goal.

Aaron Sequeira, my secondary supervisor, without whom I would have been lost in the myriad of this topic. From conducting the experiment together, where we may or may not have endangered 20,000 EUR worth of lab equipment, to every single meeting we have had, has taught me so much, and I was able to fit more and more pieces to the jigsaw puzzle of my thesis. I am extremely grateful for all of the guidance that I received, which helped me shape my thesis till the very end.

Rhea Liem, my professor and mentor back in HKUST, who gave me access to so many opportunities and advice that definitely helped shape my perspective during my undergraduate studies.

To all my friends here in Delft, especially the AWE support group, with whom I discussed everything under the sun - from assignments to F1 to random outings, I am truly grateful. A special mention to Gokhul, whom I could rely on for all my doubts in acoustics and PDE.

To my friends, Anhad, Siddhant and Shriya - every single call, text and moronic conversation just kept me going much more than you can possibly imagine. You guys provided me a sense of comfort even from the other side of the world.

I would like to thank my parents and my sister, not just for standing behind me through thick and thin, but for providing all the love and support when things were not going my way. I will forever be indebted to you. And a special mention to baby Vihani, my sister's newborn, whose adorable smile gave me the much-needed serotonin boost while I was working late at night.

Finally, I am grateful to the Almighty, Kanchi Mahaswami, for all the eternal blessings, strength and protection that I have been bestowed upon during my journey.

Srivatsav Swaminathan
December 2025

Summary

Over the past few decades, aircraft design priorities have shifted from maximising cruise speed to reducing fuel burn and emissions. Rising fuel costs, environmental regulations, and the emergence of electric and hybrid-electric propulsion have renewed interest in propeller-driven concepts, such as Distributed Electric Propulsion. These concepts often involve placing multiple propellers in proximity to each other or close to other aerodynamic surfaces. As such, there exists a need to better understand the behaviour of the boundary layer on downstream surfaces.

At the moderate chord Reynolds numbers relevant here, laminar–turbulent transition, boundary layer separation and the formation or suppression of LSBs can alter lift, drag, stall margins and noise. LSBs arise when a laminar layer separates, transitions within a free shear layer and then reattaches, resulting in a turbulent flow. A propeller modifies this flow field by generating a non-uniform, unsteady slipstream consisting of accelerated axial flow, swirl, and a helical system of tip and root vortices and blade wakes. The resulting spatially and temporally varying inflow alters local incidence, dynamic pressure and boundary layer dynamics over the wing. Existing studies rely primarily on time-averaged measurements and lack sufficient spatial and temporal resolution near the wall. As a result, the detailed mechanisms by which helical vortices and wake sheets interact with the downstream boundary layer, their spanwise variation within and around the slipstream core, and their influence on LSB dynamics remain only partially understood.

The present thesis aims to provide an experimental characterisation of how a propeller slipstream modifies a downstream laminar boundary layer behaviour. Two complementary campaigns have been used to answer the research objective: oil-flow visualisations and acoustic measurements on the surface of an airfoil placed under a propeller slipstream to understand the time-averaged boundary layer in a global sense, and a local, high-resolution investigation using phase-locked stereoscopic Particle Image Velocimetry (sPIV) to resolve the vortex structures within the slipstream and understand their effect on the boundary layer. Together, these experiments address the questions of (i) how the slipstream alters laminar–turbulent transition and LSB formation, and (ii) what role unsteady vortical structures within the slipstream play in triggering and modulating transition along the span.

The results show that the propeller slipstream strongly energises the downstream boundary layer and generally promotes earlier transition, but in a manner that is highly non-uniform in both span and blade-passage phase. The results indicate that under a propeller slipstream, transition is advanced and the boundary layer thickens on the inboard side, where inboard shearing and higher slipstream velocities amplify near-wall turbulence. The slipstream also modifies LSB behaviour, and depending upon slipstream amplitude and effective local incidence angle, the LSB may be suppressed entirely, shortened and displaced upstream, or persist within regions of weaker propeller loading. Phase-locked sPIV reveals that these behaviours are governed by an intrinsically three-dimensional, intermittent interaction between the boundary layer and a coupled system of primary tip vortices, secondary wall-originating vortices and blade wakes. Wake-impingement events generate short bursts of high shear and TKE separated by phases of weakly turbulent or nearly laminar near-wall flow. Comparable TKE levels for tripped and untripped cases at the same wall-normal position show that near-wall turbulence inside the slipstream is dominated by the imposed unsteady forcing rather than by the state of the boundary layer.

Contents

List of Figures

Nomenclature

Abbreviations

Abbreviation	Definition
AOA	Angle of Attack
APG	Adverse Pressure Gradient
ATP	Advanced Turboprop Project
BPF	Blade Passing Frequency
DAQ	Data Acquisition
DEP	Distributed Electric Propulsion
ESC	Electronic Speed Controller
eVTOL	electric Vertical Take-Off and Landing
FOV	Field of View
IRT	Infrared Thermography
K-H	Kelvin - Helmholtz
LSB	Laminar Separation Bubble
OFV	Oil Flow Visualisation
PCB	Printed Circuit Board
PIV	Particle Image Velocimetry
PSD	Power Spectral Density
PTU	Programmable Timing Unit
RMS	Root Mean Square
RPM	Rotations Per Minute
RPS	Rotations Per Second
SES	Sensor Embedded Sleeve
SLT	Small Low Turbulence
sPIV	Stereoscopic PIV
SPL	Sound Pressure Level
TKE	Turbulent Kinetic Energy
UV	Ultraviolet

Symbols

Symbol	Definition	Unit
C_P	Power coefficient	[-]
C_Q	Torque coefficient	[-]
C_T	Thrust coefficient based on n, D_P and ρ_∞	[-]
T_c	Thrust coefficient based on freestream velocity V_∞	[-]
D_P	Propeller diameter	[m]
f	Frequency	[Hz]
f_{rev}	Propeller rotational frequency	[Hz]
J	Advance ratio	[-]
n	Propeller rotational speed (shaft rotation rate)	[Hz]
P	Power delivered to the propeller	[W]
p	Static pressure	[Pa]
p_{rms}	Root-mean-square pressure fluctuation	[Pa]
Q	Propeller torque	[N m]
R	Propeller radius	[m]
Re_c	Reynolds number based on chord c	[-]
Re_δ	Reynolds number based on boundary-layer thickness δ	[-]
T	Thrust	[N]
Δt	Inter-frame time between PIV image pairs	[s]
Δz	Spanwise spacing between PIV measurement planes	[m]
U	Time-averaged streamwise velocity component	[m/s]
U_∞	Freestream velocity in the wind tunnel	[m/s]
u	Streamwise velocity component	[m/s]
v	Wall-normal velocity component	[m/s]
w	Spanwise velocity component	[m/s]
α	Angle of attack	[deg]
β	Blade pitch angle	[deg]
δ	Nominal boundary-layer thickness	[m]
δ_{99}	Boundary-layer thickness at 99% of U_∞	[m]
η_p	Propulsive efficiency of the propeller	[-]
ϕ	Propeller azimuth / phase angle	[deg]
ρ	Air density	[kg/m^3]
ρ_∞	Freestream air density	[kg/m^3]
ω_y	Wall-normal (y-component) vorticity	[1/s]

1

Introduction

In the early stages of aviation, with the introduction of high transonic speed aircraft and supersonic aircraft such as the Concorde, aircraft manufacturers were primarily focused on designing aircraft which could fly as fast as possible. However, the 1973 oil crisis and greater awareness of the effects of climate change caused a paradigm shift in the entire aviation industry to tackle the rising costs of oil while also making aircraft more efficient and sustainable. This resulted in a re-evaluation of propeller-based aircraft due to their higher propulsive efficiencies as compared to conventional turbofan engines. The Advanced Turboprop Project (ATP) led by NASA in partnership with Boeing in the 1980s demonstrated highly efficient propellers that could achieve cruise speeds of Mach 0.65 to 0.85, comparable to typical cruise speeds of turbofan aircraft, while also projecting a reduction of approximately 40 to 50 percent in fuel consumption [1].

In recent years, the emergence of electric and hybrid-electric propulsion aircraft has once again renewed interest in propeller-driven aircraft. With increasing societal pressure to decarbonise the aviation industry, concepts such as Distributed Electric Propulsion (DEP) and ultra-efficient regional aircraft have brought propellers to the forefront of aerodynamic research. These propulsion systems often involve multiple propellers in proximity to each other or propellers in proximity to aerodynamic surfaces such as the wing or tailplane, or even other control surfaces such as ailerons and flaps [2]. As a result, there exists a need to better understand how the propeller slipstream affects the airflow over surfaces downstream of the propeller.

Accordingly, there is growing recognition that a purely steady description of slipstream–surface interaction is insufficient. The time-averaged velocity field and swirl set the baseline modification of lift, drag, and stall margins on downstream surfaces, but these are always accompanied by strongly periodic and broadband unsteady structures associated with blade passage, vortex shedding, and their interaction with the local boundary layer. The unsteady component can promote or delay separation, alter transition behaviour, and generate fluctuating loads and noise that are critical for structural fatigue, handling qualities, and passenger comfort. A comprehensive understanding therefore, requires joint consideration of both the steady alteration of the mean flow and the superposed unsteady response of the boundary layer and wake, motivating a more detailed examination of the unsteady propeller slipstream and its interaction with nearby lifting surfaces.

Within this renewed landscape, a central question is how the unsteady propeller slipstream interacts with nearby lifting surfaces. The helical wake and blade-passage disturbances impose spatially and temporally varying inflow on downstream surfaces, altering boundary-layer growth, separation tendency, and the onset of turbulence. These effects govern drag, noise, and control effectiveness,

and they become especially pronounced when propellers are placed close to wings or high-lift devices, as is typical in distributed-propulsion or tractor configurations.

The work done in this thesis study provides an experimental characterisation of both the steady and unsteady effects of the propeller slipstream interaction with a downstream boundary layer using two complementary experimental campaigns. The first experiment examines global transition and separation behaviour on an airfoil under the effect of a propeller slipstream using surface microphones measuring hydrodynamic pressure fluctuations and Oil Flow Visualisation (OFV). Further to this, local, highly resolved measurements of the slipstream interaction are conducted for a laminar boundary layer developing over the leading edge of a flat plate using time-averaged and phase-locked stereoscopic Particle Image Velocimetry (sPIV) to understand the unsteady effects of the slipstream interaction. Together, the two campaigns aim to answer how boundary layer characteristics change under the influence of a propeller slipstream, investigate Laminar Separation Bubble (LSB) characteristics and understand the inherent vortex structures within the propeller slipstream, thereby providing experimentally grounded insight that is directly applicable to the aerodynamic design and integration of propeller-driven high-lift systems in future low-emission aircraft.

The remainder of this thesis is organised as follows. The next chapter introduces the fundamental concepts required to contextualise the study, followed by a critical review of the existing literature that identifies unresolved issues and motivates the research objectives. The Methodology chapter then details the two experimental campaigns, including instrumentation, test conditions, and data-processing workflows. Results and discussion are presented in two parts, corresponding to the first and second campaigns, where the experimentally acquired data has been processed and interpreted to answer the research questions that were set out. Finally, the Conclusions chapter synthesises the principal findings with respect to the research questions, acknowledges the study's limitations, and outlines directions for future work.

2

Literature Review

This chapter discusses the fundamental principles required to understand the work done in this thesis along with a review on existing literature, eventually, leading to the motivation of this study and the research questions.

2.1. Boundary Layer

The study of fluid motion, particularly in boundary layers, is central to understanding many aerodynamic and hydrodynamic phenomena. The Navier–Stokes equations provide the fundamental mathematical framework for modelling viscous flows, but their direct application to high–Reynolds number configurations around bodies is often intractable. Ludwig Prandtl's boundary layer theory, introduced in 1904, resolved this difficulty by recognising that, at high Reynolds numbers, viscous effects are confined to a thin region adjacent to the solid surface, while the bulk of the flow can be treated as essentially inviscid [3]. Prandtl's theory divides the flow into two regions - the outer region, governed to good approximation by the inviscid Euler equations, and an inner region, the boundary layer, in which viscosity, strong velocity gradients, and wall shear stresses are dominant.

Within the boundary layer, the fluid velocity increases rapidly from zero at the wall (no-slip condition) to nearly the free-stream value over a small distance normal to the surface. This thin viscous layer introduces new length scales, such as the boundary layer thickness and the displacement and momentum thicknesses, which quantify how the presence of the wall and viscous shear modify the outer flow. Depending on the Reynolds number and surface conditions, the boundary layer can be laminar or turbulent, with the latter exhibiting enhanced momentum transfer and higher skin-friction drag. Under an adverse pressure gradient, the boundary layer may separate from the surface when the near-wall fluid is no longer able to overcome the increasing pressure, leading to large changes in lift and drag. Prandtl's concept of a thin viscous layer interacting with an outer inviscid flow thus provides both a physical and mathematical framework for analysing wall-bounded flows and underpins much of modern aerodynamic theory.

The motion of a Newtonian fluid can be classified into three states - laminar, turbulent and transition states.

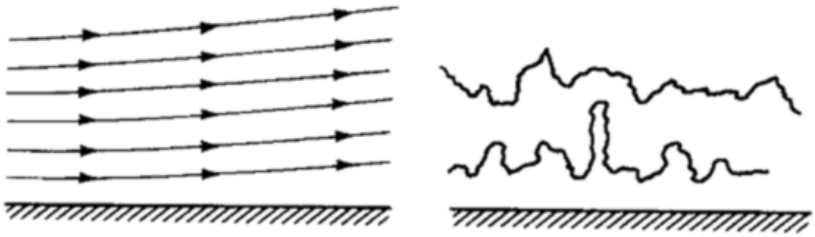

Figure 2.1: Laminar flow (left) and Turbulent flow (right) [4].

A flow is classified as laminar when the pathlines of fluid elements remain smooth and orderly, resulting in predictable motion, while turbulent flow is characterised by random, chaotic fluctuations, as illustrated in Figure 2.1. In turbulent flow regimes, shown in Figure 2.2, the irregular and energetic motion significantly enhances the momentum transfer among fluid particles. This increased mixing leads to the formation of vortical structures, whose generation, evolution, interaction, and eventual dissipation dominate the dynamics of turbulent fields. Within a turbulent boundary layer, such chaotic motion transports high-energy fluid from the outer flow region toward the near-wall region, particularly close to surfaces such as an airfoil. Consequently, turbulent flows exhibit higher velocities near the surface compared to laminar flows, driven by the intense mixing of fluid parcels from different flow regions and the associated vortical activity.

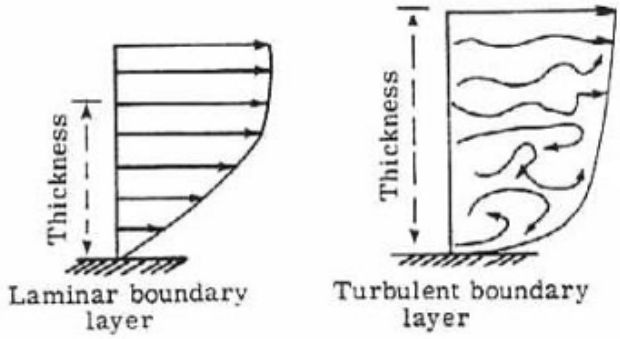

Figure 2.2: Laminar and turbulent velocity profiles [4].

The generation of these vortical structures occurs during the transitory phase from laminar to turbulent flow, where the initially stable laminar boundary layer becomes susceptible to disturbances. The amplification of instabilities governs this process, typically Tollmien-Schlichting waves in low-disturbance environments, which grow in magnitude until non-linear effects cause the breakdown into turbulence [5]. The transition does not occur instantaneously; rather, it spans a finite region downstream of the disturbance origin, commonly referred to as the transition region, as illustrated in Figure 2.3.

Within this region, localized patches of turbulent flow, termed turbulent wedges, begin to emerge and grow spatially in both the streamwise and spanwise directions. These wedges are initiated by small perturbations or surface irregularities and are characterized by intense shear and vorticity. As they expand, they interact and eventually coalesce, leading to the formation of a fully turbulent boundary layer. The precise location and nature of transition are highly sensitive to freestream turbulence, surface roughness, pressure gradients, and other environmental factors, making it a complex and critical phenomenon in aerodynamic design and analysis [6].

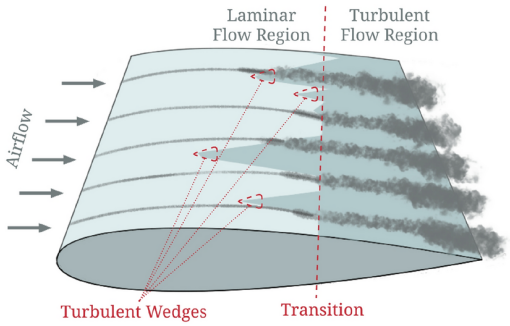

Figure 2.3: Laminar, transition and turbulent regions over an airfoil [7].

Another fundamental principle that warrants discussion in this text is the concept of boundary layer separation. Boundary-layer separation arises when the near-wall flow can no longer overcome an adverse pressure gradient. Within the boundary layer, viscous effects continuously extract kinetic energy from the flow and convert it into heat, leading to a progressive loss of momentum. When an adverse pressure gradient is imposed, the outer flow decelerates and the boundary-layer profiles become increasingly "less full" and may develop an inflection point. If the pressure gradient exceeds the local momentum available in the near-wall region, the fluid is unable to follow the surface, the wall shear stress vanishes, and the flow reverses locally: the boundary layer then detaches and separation occurs [8]. A schematic of a separating boundary layer has been shown in Figure 2.4.

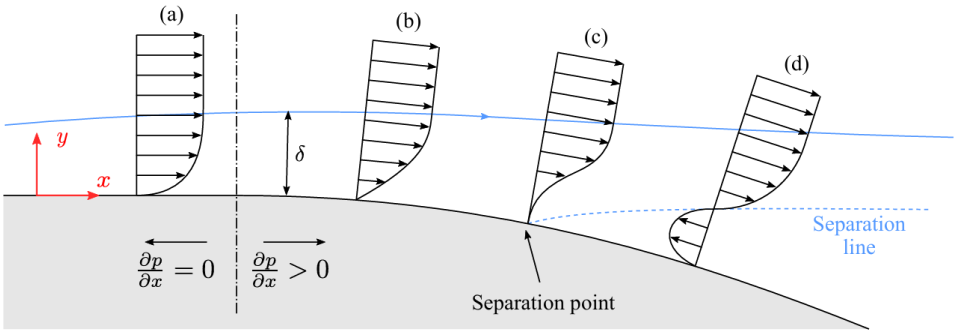

Figure 2.4: Schematic of boundary layer separation [8].

The separated region is characterised by low velocity and relatively high pressure, forming a recirculating zone bounded by a separation line across which there is no mass flux. For aerodynamic applications, this leads to a loss of lift and a significant increase in pressure drag. The state of the boundary layer strongly influences separation behaviour: a turbulent boundary layer, which carries more momentum close to the wall, can generally withstand stronger adverse pressure gradients and remain attached further downstream than an equivalent laminar boundary layer. In both laminar and turbulent cases, separation is inherently unsteady, with instabilities in the separated shear layer giving rise to large-scale vortical structures and periodic vortex shedding.

Boundary-layer separation can manifest in several forms depending on the surrounding flow field. One particularly relevant example is the formation of a LSB. When laminar boundary layers separate due to the presence of an adverse pressure gradient, the separated shear layer undergoes laminar to turbulent transition. The latter increases momentum exchange between the inner and outer parts of the shear layer. If the momentum exchange is adequate for counteracting the adverse pressure gradient, reattachment is observed. This results in the formation of a wall-bounded closed

recirculation region, known as a laminar separation bubble. The schematic of a LSB is shown in Figure 2.5.

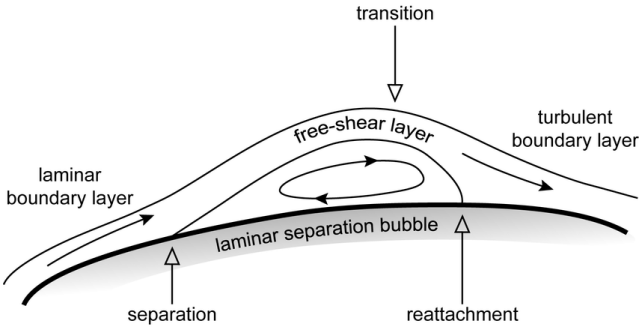

Figure 2.5: Schematic of a laminar separation bubble.

The state of the boundary layer is one of the primary factors controlling aerodynamic performance. The distribution of skin–friction and pressure over lifting surfaces determines lift, drag and pitching moment characteristics, and hence directly impacts fuel consumption, emissions and attainable flight envelopes. Laminar boundary layers are associated with lower skin–friction drag but are highly sensitive to disturbances and adverse pressure gradients, making them prone to early separation and abrupt stall. Turbulent boundary layers, in contrast, incur higher skin–friction drag but can better resist adverse pressure gradients and delay separation, often providing more benign and predictable stall behaviour. The location of transition, the onset and extent of separation, and the possible formation of laminar separation bubbles therefore govern maximum lift, stall margins, control-surface effectiveness and, in many cases, aeroacoustic emissions.

These considerations are particularly important for the flow configurations targeted in the present thesis. The surfaces of interest operate at relatively low Reynolds numbers, where laminar–turbulent transition and LSBs are common, and where even modest changes in pressure gradient or disturbance environment can trigger large changes in separation behaviour. In such regimes, any mechanism that modifies the boundary-layer state, in this case, unsteady forcing and non-uniform inflow associated with a propeller slipstream, can substantially alter the transition location, the formation or suppression of LSBs, and the position of separation and reattachment. Understanding how the boundary layer responds to these effects is therefore essential for predicting and controlling lift, drag and stall characteristics of propeller-driven configurations, and motivates the experimental investigations presented in this thesis.

2.2. Propeller Aerodynamics

A propeller is a device that generates thrust by accelerating incoming air through the rotation of blades around a fixed hub and expelling the accelerated air behind the blades. Each propeller blade has an airfoil-shaped cross-section, which supports a circulation and an associated pressure difference between its suction and pressure sides. Through its rotation, the propeller performs mechanical work on the flow, increasing the total pressure and imparting both axial and tangential momentum, thereby generating thrust. The forces experienced by a propeller can be resolved into two components - thrust and torque. This has been illustrated in Figure 2.6.

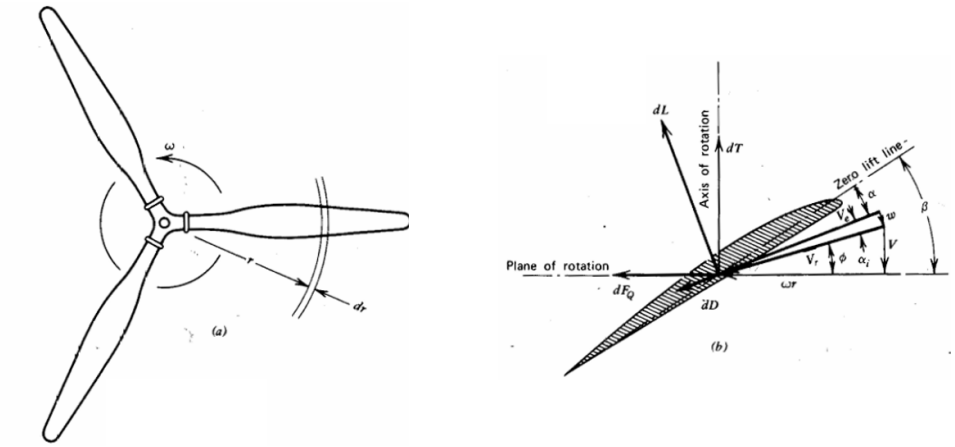

Figure 2.6: Velocities and forces acting on a propeller blade [9].

Using Newton's third law, it is possible to derive an expression for the thrust produced by a propeller based on the mass flow rate through the propeller, the freestream velocity, and the exhaust jet velocity. This relationship is given in Equation 2.1. The propulsive efficiency, defined as the ratio of useful propulsive power to the rate at which kinetic energy is added to the flow, is presented in Equation 2.2. In these equations, V_e is the velocity of the exiting jet at the nozzle exit, and V_∞ is the freestream velocity.

$$T = \dot{m}(V_e - V_\infty) \tag{2.1}$$

$$\eta_p = \frac{2}{1 + \frac{V_e}{V_\infty}} \tag{2.2}$$

In order to produce an equivalent amount of thrust, either a large mass of incoming air must be accelerated with a small change in velocity or a small mass of air must be accelerated with a large change in velocity. As indicated by Equation 2.2, propulsive efficiency increases when the velocity difference is minimized. Therefore, greater efficiency is achieved when a large volume of air is accelerated by a small change in velocity. This is a key reason why propellers generally attain higher propulsive efficiencies than jet engines. Jet engines require the use of an external cowling, which adds both weight and drag [10]. In contrast, propellers are capable of ingesting a larger mass flow of air, which contributes to their superior efficiency.

To compare the aerodynamic characteristics of various propellers, several non-dimensional performance coefficients can be introduced. The thrust generated by the propeller, denoted by T, can be non-dimensionalised in two common ways. One approach involves the use of the rotational speed n, propeller diameter D_P, and freestream density ρ_∞, as shown in Equation 2.3. Alternatively, the freestream velocity V_∞ may replace the rotational speed in the non-dimensionalisation, as demonstrated in Equation 2.4. Similarly, the power and torque of the propeller can be expressed in non-dimensional form, as shown in Equation 2.5 and Equation 2.6, respectively.

$$C_T = \frac{T}{\rho_\infty n^2 D_P^4} \tag{2.3}$$

$$T_C = \frac{T}{\rho_\infty V_\infty^2 D_P^2} \tag{2.4}$$

$$C_P = \frac{P}{\rho_\infty n^3 D_P^5} \tag{2.5}$$

$$C_Q = \frac{Q}{\rho_\infty n^2 D_P^5} \tag{2.6}$$

Another important non-dimensional parameter in the analysis of propeller performance and propeller–wing interaction is the Advance Ratio. This parameter non-dimensionalises the propeller's rotational speed using the freestream velocity, as defined in Equation 2.7 [11]. Physically, the advance ratio can be interpreted as the axial distance travelled by the aircraft during one full revolution of the propeller.

$$J = \frac{V_\infty}{n D_P} \tag{2.7}$$

With the definitions of C_T, C_P, and J now established, the propeller efficiency can be expressed as shown in Equation 2.8:

$$\eta_p = \frac{C_T J}{C_P} \tag{2.8}$$

2.3. Propeller Slipstream

In order to understand the flow around a propeller–wing configuration, it is first necessary to characterise the propeller slipstream in isolation. As illustrated in Figure 2.7, the rotating blades act as a lifting system that modifies the incoming flow, producing a contracted streamtube and an associated vortex system. The blade loading generates bound circulation, and the corresponding vorticity is shed into the wake; through self-induction this wake vorticity rolls up into concentrated helical vortices at the blade tips and roots, in direct analogy with the vortex system of a finite wing. The resulting slipstream therefore consists of both the blade wakes and the tip- and root-vortex structures, which together induce predominantly an axial velocity component V_a and a tangential (swirl) component V_t. Viscous boundary layers on the blades are the source of the vorticity feeding this wake–vortex system, so regions of enhanced shear and velocity deficit are also present within the slipstream [12].

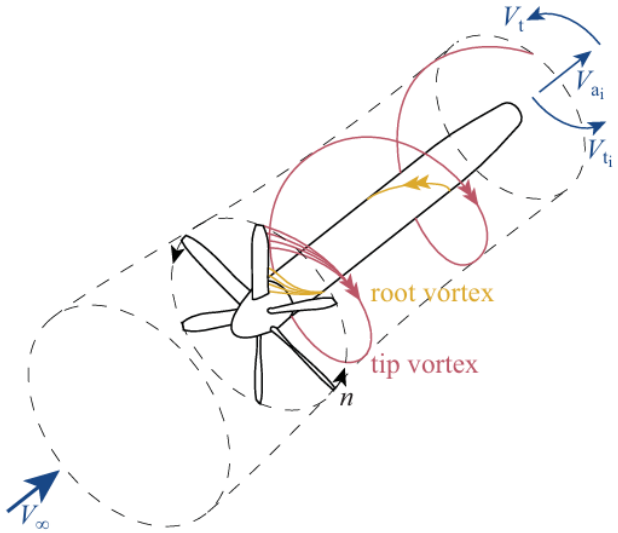

Figure 2.7: Propeller Streamtube and Vortex System [12]

The axial velocity component refers to the portion of the flow velocity that is aligned with the propeller's thrust axis. Along the span of the blade, this axial velocity exhibits strong gradients due to the non-uniform distribution of aerodynamic loading. The axial velocity generally reaches its peak around the 0.75R position, where R is the propeller radius. Near the blade root and tip, where the loading is minimal, the axial velocity also tends to be lower, as illustrated in Figure 2.8a. As the flow progresses downstream of the propeller, the axial velocity increases primarily due to pressure recovery between the propeller disc and the far wake, with the associated slipstream contraction arising as a consequence of mass conservation, as shown in Figure 2.8b. This progressive axial acceleration in the wake is central to propeller–wing interaction, because it determines the local dynamic pressure and its streamwise gradients at the wing location, and thus strongly influences the additional lift, loading distribution, and boundary-layer behaviour for a given longitudinal propeller–wing spacing.

In addition to the axial velocity increase, the rotating propeller generates an azimuthal (tangential) velocity component in the flow. The representative distribution of swirl velocity along the blade span, expressed in V_t/V_∞, is shown in Figure 2.8a. This tangential component is particularly important for propeller–wing interaction because the local inflow at the wing is given by the vector sum of the axial and tangential velocities, so the swirl rotates the incoming velocity vector relative to the wing chord. Depending on whether a given wing section lies on the upgoing or downgoing blade side, this rotation increases or decreases the effective Angle of Attack (AOA), thereby modifying the local lift, stall margin, and boundary-layer behaviour, and hence the overall aerodynamic performance.

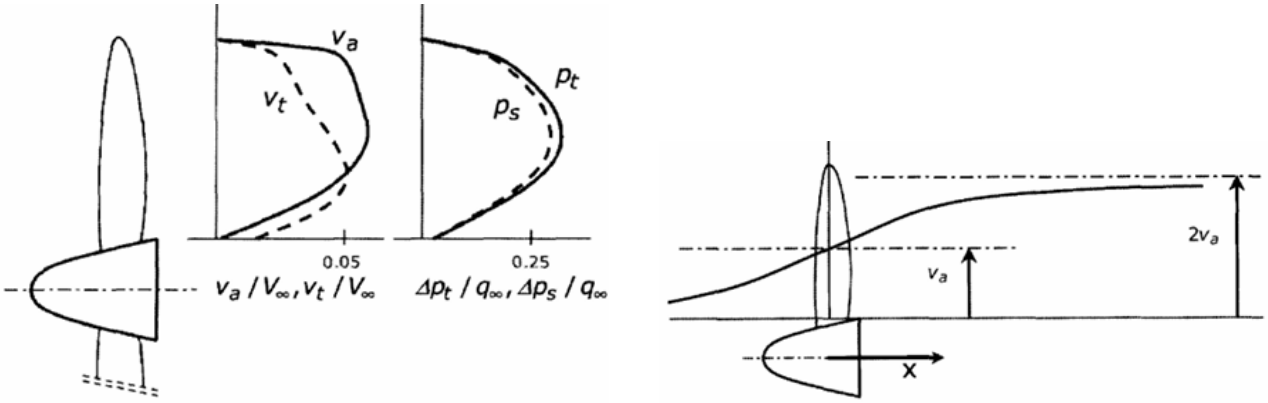

(a) Axial and tangential velocity profiles along a blade

(b) Streamwise variation of slipstream axial velocity

Figure 2.8: Velocity variation in the spanwise and streamwise directions [13]

2.4. Review of Existing Literature

The interaction between propeller slipstream and wing boundary layer has been studied extensively in the past and is crucial in determining aerodynamic performance. The unsteady, high-energy wake generated by rotating blades introduces complex flow phenomena that can significantly affect the laminar-turbulent transition behaviour on downstream surfaces. The knowledge obtained from the studies involving the interaction is particularly important in the field of aircraft design to optimally place the propellers in proximity to the lifting surfaces.

Early foundational work by Miley and Holmes provided a conceptual model of the slipstream-boundary layer interaction, identifying how the helical wake of the propeller places induces patches of turbulence that intermittently disturb the laminar regions over the wing [14]. While there was no direct flow visualisation, a schematic was made as shown in Figure 2.9 which was constructed by correlating data from both flight and wind tunnel tests. Figure 2.9 highlights the spatially varying nature of these disturbances which are phase-locked to the propeller. The trailing vortices are convected downstream and periodically intersect the wing, creating localised patches of turbulence within the otherwise laminar boundary layer.

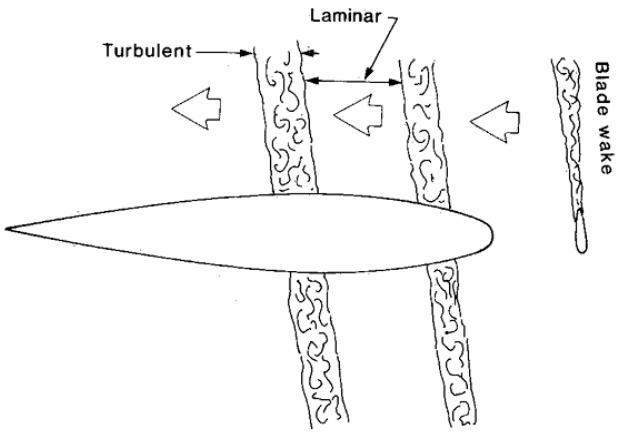

Figure 2.9: Slipstream Disturbance in Flow [14]

Subsequent investigations have quantified how slipstream effects promote early transition, with studies demonstrating that laminar flow can be reduced by up to 80% when a wing is immersed in

propeller wake [15]. This is especially pronounced for low Reynolds number or laminar airfoils, where transition is pushed toward the leading edge due to heightened local turbulence levels. Figure 2.10 presents the results obtained by Catalano et al. [15] where it is evident that with an increase in AOA, the transition front was brought closer to the leading edge until turbulence was observed at the leading edge of the wing.

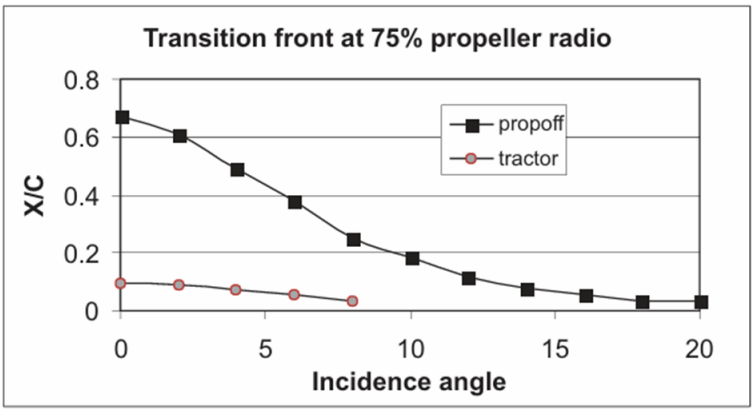

Figure 2.10: Transition Location in Tractor Configuration [15]

There was also an experiment conducted on NACA 6-series airfoils at low Reynolds numbers, which has not only confirmed this trend but has also shown that increasing the propeller RPM causes the turbulent region to extend over most of the wing surface [16]. The propeller-induced upwash and swirl also lead to spanwise variation in pressure distribution, thereby altering the lift characteristics and wing loading.

More recently, non-intrusive techniques like infrared thermography (IRT) have been employed to detect boundary layer transition by correlating surface temperature differences to flow regime, as demonstrated in scale-model eVTOL experiments [17]. As shown in Figure 2.11, laminar boundary layers convect less heat away from the wall as compared to turbulent boundary layers, allowing time-averaged thermal images to capture transition patterns even in highly three-dimensional slipstream-affected flows. From the figure, it can be seen that there is an earlier onset of transition after the propeller is switched on. The earlier onset of transition is a result of the increased turbulence in the propeller wake and the increased Reynolds number compared to the undisturbed wind tunnel flow.

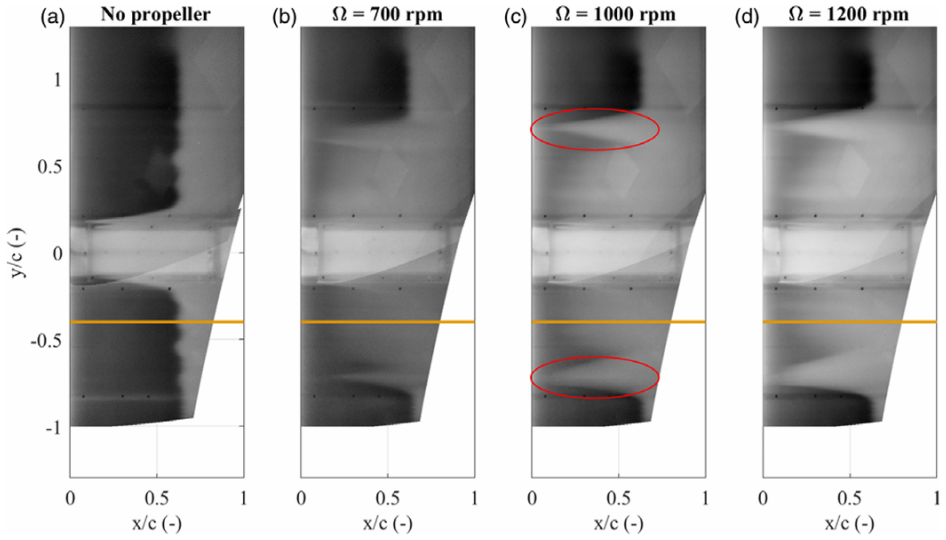

Figure 2.11: Average Intensity Distributions at $\alpha = 2.5°$ and $U_\infty = 40m/s$. The trailing vortices of the propeller blades have been highlighted in red. Orange lines are at a fixed spanwise position of y/c of 0.4 and are used as a reference point for another image [17].

Apart from increasing background turbulence levels and promoting earlier transition, the slipstream also contains coherent, phase-locked structures (blade wakes, tip and root vortices) whose repeated impingement on the surface governs much of the near-wall unsteadiness downstream. Both the broadband turbulent fluctuations and the coherent vortices can contribute to advancing transition: the former by raising the disturbance environment in which the boundary layer develops, and the latter by injecting periodic, high-amplitude perturbations at the blade-passage frequency and its harmonics. Together, these mechanisms control not only the mean transition location (Figure 2.10, Figure 2.11) but also the instantaneous spatial footprint of the wake on the wing, and thus the detailed structure of the slipstream–boundary-layer interaction considered in this study.

The effect of the slipstream on transition represents only one aspect of the broader unsteady aerodynamics induced by the propeller. As the helical tip vortices impinge on the wing, they trigger dynamic deformations and pressure fluctuations that cannot be explained by steady considerations alone. Flow visualisation studies have therefore focused on capturing these unsteady mechanisms, revealing how vortex–wing interactions evolve in both chordwise and spanwise directions. At the leading edge of the wing, which was placed downstream of the propeller, a spanwise deformation of the tip vortex was observed [18]. This effect was attributed to inviscid interactions at the impingement point near the LE, after which viscous influences became dominant and progressively sheared the vortex filament in the spanwise direction. The deformation produced chordwise and spanwise displacements that occurred in opposite directions on the upper and lower wing surfaces [19]. In addition, the study reported a reduction in chordwise pressure fluctuations, which was linked to the breakdown of coherent vortex structures as they increasingly interacted with the wing boundary layer. Finally, it was observed that the tip vortex exhibited asymmetric stretching or thickening on either side of the wing, with the extent and direction of this effect depending on the sense of propeller rotation [20].

A comprehensive experimental framework for the tip-vortex/wing encounter was later established by Felli [21], who showed that the interaction proceeds robustly in three phases that are largely insensitive to moderate changes in advance ratio, provided the upstream wake is still coherent. First, in the approach phase, the incident tip vortex undergoes a combined streamwise bending (due to rising static pressure towards the stagnation region) and spanwise bending (image-vortex

effect), while a sheet of opposite-sign vorticity is induced at the leading edge. Secondly, during penetration, the incident vortex wraps around the leading edge and splits into pressure- and suction-side branches that undergo severing, meandering and intermittent double-helix breakdown, with a marked asymmetry driven by image-vortex and pressure-gradient effects. Finally, in the reconnection phase, the two branches rejoin downstream via a reconnecting filament, re-forming a coherent structure. This three-phase picture reconciles earlier visualisations of spanwise deformation and asymmetric stretching on the two sides of the wing and offers a physical template to interpret phase-locked PIV/TKE maps used later in the context of this thesis.

Consistent with the tip-vortex behaviour, the blade trailing-edge wake exhibits an analogous encounter–penetration–reconnection sequence upon impingement, so that thin wake sheets periodically impose high-shear filaments whose instantaneous footprints can appear as localised 'patches' of elevated or depressed TKE within an otherwise fully turbulent time-average [21]. A later study employed the use of PIV to quantify the spanwise deformation induced by the impingement of the propeller slipstream on the leading edge of the pylon [22]. The measurements revealed that the tip vortex approached the pylon at an oblique angle, bending around the leading edge before progressively splitting along the chord. At this point of impingement, localised spanwise displacements were observed, which occurred independently of the more gradual spanwise displacement of the vortex trajectory along the pylon chord, the latter being driven by lift variations across the span of the pylon. Phase-locked PIV further confirmed that the tip vortex remained coherent during impingement, generating strong localised pressure fluctuations at the leading edge, which decayed downstream as viscous interactions with the boundary layer weakened the vortex core.

Another aspect of the propeller slipstream that complements the change in flow regimes is the formation of the LSB. At the low chord Reynolds numbers relevant to this study, LSBs can form on the suction side of an airfoil when a laminar boundary layer separates under an adverse pressure gradient, transitions to turbulence in a free shear layer, and subsequently reattaches [23]. In the absence of a propeller, such bubbles typically occur near the leading edge and strongly influence stall onset, lift curve slope, and unsteady loading. When a propeller slipstream impinges on the wing, the local boundary-layer environment is modified by three coupled effects: an increase in dynamic pressure and chordwise Reynolds number, a substantial rise in turbulence intensity due to blade wakes and tip vortices, and changes in the effective incidence and pressure distribution. Experimental studies on installed propeller–wing configurations at comparable Reynolds numbers show that, within the core of the slipstream, the elevated turbulence and velocity generally suppress or "wash out" the suction-side LSB and promote an attached turbulent boundary layer, while outside the slipstream the flow can remain laminar and still form an LSB with modified position and extent [24]. The resulting pattern is a spanwise non-uniform mixture of turbulent, bubble-free regions and laminar–separation–bubble regions, whose exact layout depends on propeller operating condition, propeller–wing spacing, and AOA. The present experiments, which resolve both the boundary-layer response on an airfoil and the slipstream structure over a flat plate, are therefore directly sensitive to how the propeller-induced velocity and turbulence fields alter LSB formation, suppression, and associated unsteady shedding on downstream surfaces.

2.5. Research Gaps and Motivation

Despite a substantial body of work, several critical gaps remain in understanding slipstream boundary layer interactions. First, much of the existing evidence is derived from time-averaged or quasi-steady datasets that smear the phase-dependent footprint of the slipstream, that smear the phase-dependent footprint of the slipstream, preventing a clear determination of how the periodic slipstream disturbances trigger and modulate the boundary layer response. In the relatively few

cases where unsteady measurements are available, the spatial and temporal resolution in the near-wall, pre-transitional region is often insufficient to resolve the onset, growth, and bursting of LSBs, or to capture the intermittent nature of transition.

Secondly, the pathway by which helical vortex systems and blade-wake sheets trigger or modulate transition remains insufficiently characterised. In particular, the relative roles of (i) periodic high-shear impingement at the blade-pass frequency, (ii) tip/root-vortex-induced crossflow, sweep/ejection events and associated near-wall intermittency, and (iii) slipstream-induced modifications to the leading-edge pressure field (e.g. altered suction peak and streamwise pressure gradient) have not been decoupled in a phase-locked, spatially resolved manner.

Thirdly, spanwise variations are insufficiently characterised. The literature rarely maps how the transitional footprint varies across the slipstream envelope from outboard to inboard stations and how the convection of vortical structures through the field of view modulates local boundary layer metrics (e.g. δ_{99} and turbulent kinetic energy). Without systematic measurements at multiple spanwise stations near the leading edge, it remains unclear whether reported transition criteria are specific to the sampled locations or representative of the slipstream-affected region as a whole.

Finally, the scarcity of high-fidelity, phase-locked datasets hampers model development. Current transition prediction approaches for flows impacted by the propeller slipstream rely on empirical corrections or time-averaged correlations, with limited validation against measurements that resolve the blade-phase, near-wall dynamics. As a result, design-relevant questions such as the sensitivity of transition location to advance ratio, blade pitch, or imposed pressure gradient remain only qualitatively addressed.

To address these gaps, the present work focuses on experimentally characterising the onset and mechanisms of transition on a flat plate exposed to a controlled propeller slipstream. Emphasis is placed on (i) phase-locked, high-resolution measurements synchronised to the blade-pass, (ii) near-leading-edge interrogation at multiple spanwise locations within and adjacent to the slipstream, and (iii) joint use of boundary-layer diagnostics (e.g. TKE, δ_{99}) alongside qualitative indicators (oil-flow visualisation and acoustic mapping) to link instantaneous helical-structure impingement to changes in surface-flow topology and transition.

2.6. Research Aim and Objectives

Based on the research gaps identified in section 2.5, the objective of this study is to address the following research questions:

1. How does the propeller slipstream influence the change in flow regime from laminar to turbulent and the formation of a laminar separation bubble in a high-lift configuration?
2. What role do unsteady vortical structures within the slipstream play in triggering boundary-layer transition, and how do they vary downstream on a wing?

In order to address the first research question, two complementary experimental set-ups are employed: one for a global, applied investigation of the propeller–wing configuration, and one that does a detailed study of the inherent vortex structures. In the global set-up, microphone-array SPL maps and oil-flow visualisation are used to survey operating conditions and delineate regions of transition, separation/reattachment, and spanwise non-uniformity on the lifting surface. In the second study, sPIV measurements near the leading edge provide local velocity fields from which metrics such as boundary-layer thickness δ_{99} and turbulent kinetic energy are derived. Together, these measurements link the global overview of the flow to the underlying near-wall flow topology.

The second question will be answered by using phase-locked sPIV from the second experimental campaign. Spanwise traverses will provide a three-dimensional sense of the slipstream structure, enabling planned identification and tracking of coherent vortical features and blade wakes as they convect downstream. The aim is to establish whether, when, and where these unsteady structures are associated with changes in boundary-layer state along the flat plate.

3

Methodology

This chapter outlines the methodology followed during the experimental campaign. The campaign was conducted in two phases, wherein:

- Phase 1 of the campaign involved quantifying the propeller slipstream on a NACA 6-series airfoil using a Sensor Embedded Sleeve (SES) with a microphone and pressure sensors, and qualitatively assessing the slipstream using OFVs. The experimental objective of this campaign was to study how the variations between AOA and Advance Ratio can influence the interaction between the propeller slipstream and the wing boundary layer.
- Phase 2 of the campaign involved conducting sPIV on a flat plate, which was placed downstream of a propeller to quantify boundary layer characteristics and flow parameters such as the velocity, vorticity and turbulent kinetic energy (TKE). The experimental objective of this campaign was to study how the vortical structures within the slipstream develop as it interacts with the downstream boundary layer in both streamwise and spanwise directions.

3.1. Phase 1 - SES and OFV Measurements

3.1.1. Experimental Set-Up

This experiment was conducted in the Small Low Turbulence (SLT) Tunnel at TU Delft, a low-speed wind tunnel that can be operated in both an open-jet and closed-jet configuration, and is designed to facilitate high-resolution measurements under controlled conditions. The purpose of this study was to investigate the influence of a propeller slipstream on boundary-layer transition phenomena along a representative airfoil surface. The airfoil was fixed on a rotatable plate, as shown in Figure 3.1a, to modify the angle of attack. Holes were drilled into the plate so that the airfoil could be manually rotated and fixed at specific angles of attack, ranging in 3-degree increments from -15° to $+15^\circ$.

A propeller–nacelle assembly was positioned upstream of the airfoil to generate a slipstream over the model that is representative of a tractor installation. The propeller had a diameter of $D = 203.2$ mm and was mounted on a sting extending from the side wall of the test section. Although the blade geometry and rotation correspond to a pusher configuration with respect to the nacelle, the airfoil is located downstream of the propeller disc and therefore experiences an accelerated “tractor slipstream”, similar to that produced by wing-mounted tractor engines on transport aircraft. The sting was vertically translatable along a pair of precision-aligned X-beams attached to the side of the test section, allowing repeatable adjustment of the propeller height with respect to the airfoil mid-span. The vertical displacement of the nacelle centreline ranged from -108 mm to $+108$ mm relative to the

airfoil leading-edge height, in increments of 12 mm, resulting in a total of 19 discrete measurement positions.

In principle, an equivalent mapping of the slipstream footprint could be obtained by traversing the SES spanwise and keeping the propeller fixed. However, the SES is attached to the airfoil surface, so relocating it would require repeated removal, re-alignment, and re-attachment of the sensor array. Traversing the propeller–nacelle assembly, therefore, provides an equivalent variation in relative slipstream–airfoil offset, while keeping the airfoil and its boundary layer unchanged between configurations; any small changes in tunnel boundary effects over the vertical traverse are considered negligible compared with the dominant influence of the local slipstream. The propeller was placed at a distance of approximately one diameter upstream of the airfoil leading edge to minimise any upstream influence of the airfoil on the propeller. As no load cell was available to quantify and correct for propeller loads, the experimental setup was deliberately designed to reduce any feedback of the airfoil on the propeller.

Figure 3.1a shows the propeller in its lowest configuration (-108 mm), while Figure 3.1b illustrates the vertical measurement scale marked along the X-beam, used for accurate positioning of the sting. This range was selected to span the entire region influenced by the propeller slipstream across the airfoil span and to enable complete mapping of the transition footprint using the SES.

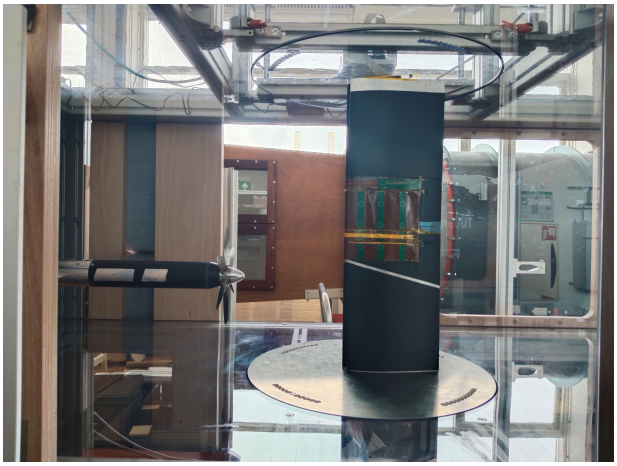

(a) Side-view of the propeller-airfoil configuration.

(b) X-beam mount showing vertical scale and sting mechanism.

Figure 3.1: Experimental setup showing the propeller mounting and vertical adjustment mechanism.

In the second phase of the experiment, surface flow behaviour was qualitatively visualised using Oil Flow Visualisation. For this phase, the SES was removed to allow direct application of oil to the airfoil surface. A fluorescent oil mixture was carefully smeared over both sides of the NACA 63_3 - 018 airfoil. With both the wind tunnel and the propeller running, the shear stress exerted by the flow caused the oil to redistribute along streamlines, thereby revealing boundary layer features such as flow attachment, separation, and laminar separation bubbles [25]. A fixed Canon DSLR camera was positioned laterally outside the test section to record time-resolved development of the oil streaks throughout the run. The flow patterns were made visible under Ultraviolet (UV) illumination, as shown in Figure 3.2. The process is repeated for every test case, and the oil mixture is reapplied to maintain uniform coverage. As the airfoil is placed in a vertical orientation in the test section, the oil motion is also affected significantly by the force of gravity. It is important to segregate the flow phenomena from the gravitational effects. For this particular test, the propeller nacelle was positioned at the 0 mm mark on the X-beam, aligning it with the airfoil mid-span to investigate the direct interaction between the slipstream core and the airfoil surface.

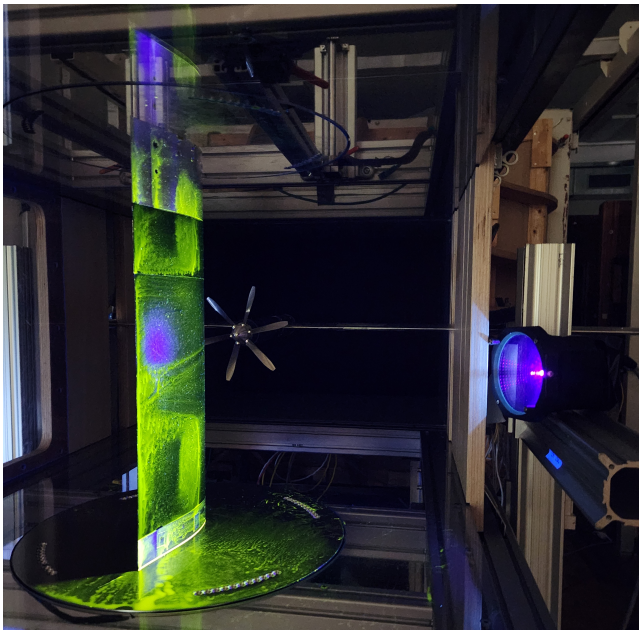

Figure 3.2: Oil Flow Visualisation setup under UV light.

3.1.2. Measurement Device - SES

The SES is a flexible PCB embedded with microphones and pressure sensors. Initial development of the Sensor Embedded Sleeve was done to investigate the effects of the propeller slipstream on the wing using a Cessna Skymaster N4207X flying testbed. The proposed design of the SES is intended to feature 54 microphones and 18 pressure sensors, designed to withstand high airspeeds of up to 80 m/s. The initial prototype design of the SES that has been used in this campaign features 18 microphones and 6 pressure sensors with dimensions of 150 $\times$ 300 mm. The data acquisition is conducted through an Ethernet cable, which also supplies power to the sensor. The microphones used are the Knowles SPW0690LM4H-1 with an operating frequency range of 45 Hz to 26000 Hz [26]. The pressure sensors are the Bosch BMP390 sensors with an operating range of 300 to 1250 hPa and an absolute and relative pressure accuracy of $\pm$ 50 Pa and $\pm$ 3 Pa, respectively [27]. The SES is not fully flexible, as the sensors require a rigid base; without it, the sensors can break off the PCB. The flexible part of the SES is Kapton-based and is designed to wrap around the leading edge of the airfoil.

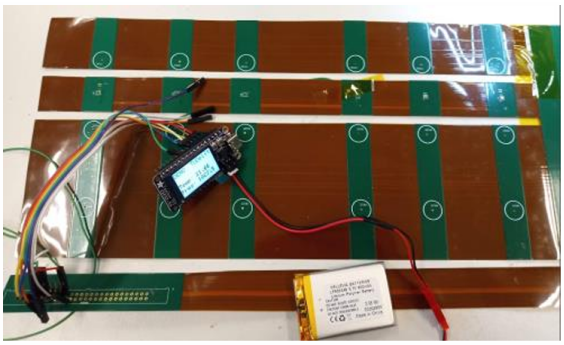

Figure 3.3: Sensor Embedded Sleeve (SES) Measurement Device.

3.1.3. Test Model

A NACA 63_3 - 018 airfoil with a chord length of 200 mm and a span length of 400 mm, extendable up to 600 mm, was used in this campaign. The airfoil has a symmetric profile with a maximum thickness-to-chord ratio of 0.18 at 0.661 x/c chord location [28]. The model is made of aluminium and has a total of 27 pressure taps distributed chord-wise on both surfaces and the data for the same has been shown in Figure 3.5.

An airfoil from the NACA 6-series was chosen due to favourable pressure recovery characteristics and extended laminar flow capability. This airfoil, in particular, is a moderately thick profile with a well-documented transition behaviour, making it suitable for studies involving slipstream-induced instabilities and boundary layer evolution.

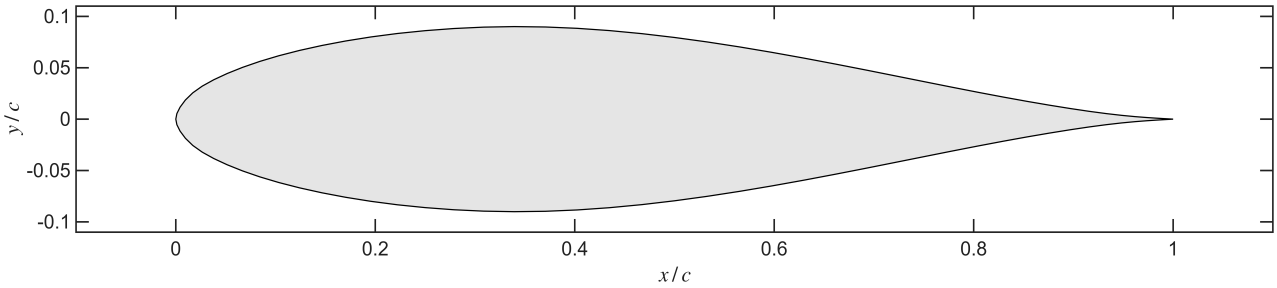

Figure 3.4: NACA 63_3 - 018 airfoil.

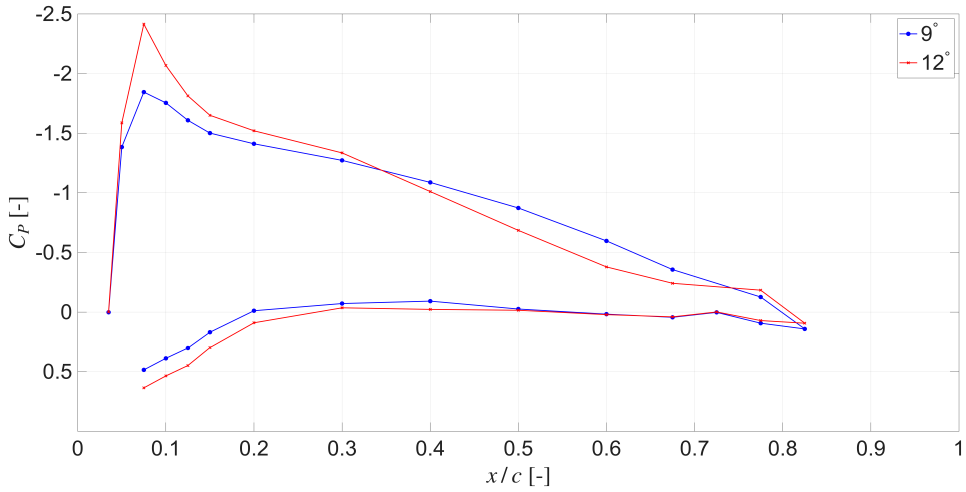

Figure 3.5: Pressure distribution of the NACA 63_3 - 018 airfoil for AOA $9°$ and $12°$. Data has been obtained from pressure taps on the airfoil model.

3.1.4. Propeller Geometry

The propeller employed in this study is the TUD-XPROP-S, a custom, six-bladed propeller with a diameter of 203.2 mm. It is a half-scale derivative of the baseline TUD-XPROP. Although direct performance measurements are unavailable for TUD-XPROP-S, its geometric similarity to TUD-XPROP implies that the principal non-dimensional performance characteristics are the same for both propellers. Accordingly, the TUD-XPROP performance data is adopted as a proxy for TUD-XPROP-S, and the thrust coefficient (T_c) versus the advance ratio has been illustrated in Figure 3.7.

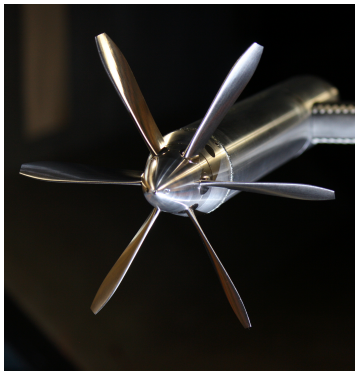

Figure 3.6: Reference photograph of the TUD-XPROP-S [29].

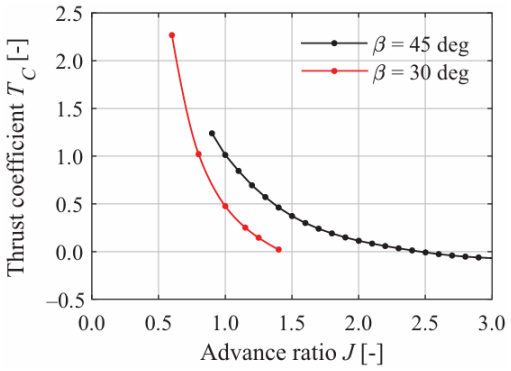

Figure 3.7: Thrust coefficient vs advance ratio for the TUD-XPROP [30].

The propeller allows for the changing of the blade pitch angle manually which influences the loading characteristics and propeller performance. Guided by the performance map in Figure 3.7, three operating points were selected to sample distinct regions of the T_c–J curve: $\beta = 30°$ at $J = 0.8$, $\beta = 45°$ at $J = 1.0$ and $\beta = 45°$ at $J = 1.8$. These settings correspond to rotational frequencies of $n = 123$ Hz, $n = 98.4$ Hz and $n = 54.7$ Hz respectively, and were chosen to produce measurably different slipstream conditions under otherwise identical inflow and geometry.

The $J = 1.0$ case was chosen in order to study the variation in advance ratio while keeping a constant T_c to that of the $J = 0.8$ case. On the other hand, while $J = 1.8$ represents a significant change in advance ratio from the original $J = 0.8$, the propeller produces a much lower T_c as compared to the $J = 0.8$ case. Subsequent inspection of the OFVs and sound-pressure-level (SPL) contour maps indicated blade stall, rendering the corresponding measurements unrepresentative of the intended operating condition. Accordingly, all $J = 1.0$ cases were excluded from further analysis and have not been discussed in chapter 4.

3.1.5. Operating Conditions and Test Cases

The test campaign was conducted at a free-stream speed $U_\infty = 20\ \mathrm{m\,s^{-1}}$, corresponding to a chord-based Reynolds number $Re \approx 2.68 \times 10^5$. Angles of attack $\alpha \in \{0°, 9°, 12°\}$ were selected to represent a baseline condition as well as a high-lift condition for the $(\beta, J) = (30°, 0.8)$ case. This case corresponded to a relatively higher thrust setting as well which is more comparable to a high-lift condition.

Two propeller operating points were targeted from the performance map (Figure 3.7): $(\beta, J) = (30°, 0.8)$, $(45°, 1.0)$ and $(45°, 1.8)$; however, as noted above, all $J = 1.0$ cases were subsequently excluded due to blade stall. Throughout, the propeller rotated anticlockwise when viewed from downstream (i.e., looking from the wing trailing edge towards the propeller).

3.2. Phase 2 - sPIV Campaign

3.2.1. Experimental Set-Up

This second experimental campaign was likewise carried out in the SLT tunnel at TU Delft, operated in an open-jet configuration. While the previous campaign (section 3.1) provided a global characterisation of the flow under the propeller slipstream using oil-flow visualisation and acoustic measurements, this experimental campaign uses sPIV to conduct a more detailed investigation of the inherent slipstream vortex structures. In particular, it examines how these vortices interact with the downstream boundary layer and how they modify its development and characteristics. Similar to the previous campaign, X95 beams were used to assemble the setup as shown in Figure 3.8.

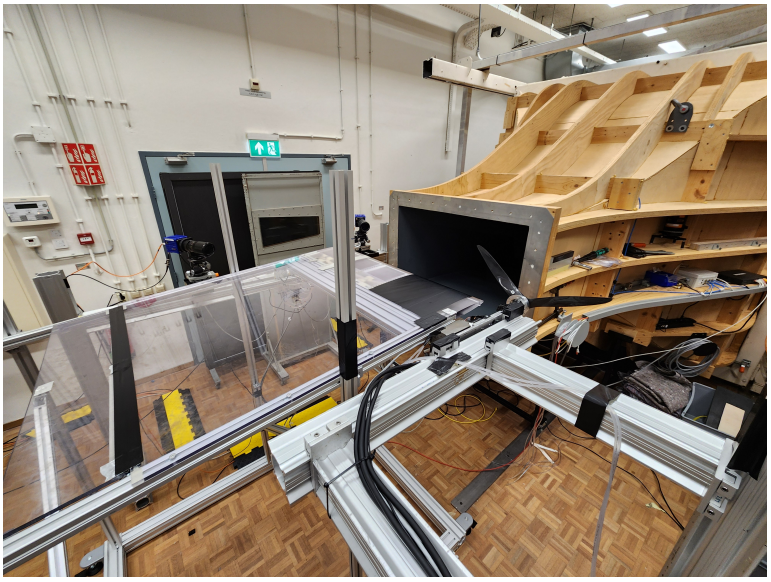

Figure 3.8: Experimental set-up for the PIV campaign.

The flat plate, propeller and drivetrain were mounted on a rigid X95-beam frame that located the entire assembly a fixed distance downstream of the nozzle exit, as indicated in Figure 3.9. A key distinction to the previous campaign (section 3.1) in this setup is the placement of the propeller with respect to the model. In the present setup, the propeller disc is semi-immersed with respect to the flat plate instead of being directly upstream of the flat plate as shown in Figure 3.9. This configuration was chosen deliberately, rather than placing the propeller fully upstream as in Phase 1. The semi-immersed arrangement effectively scales up the local interaction between the slipstream and the boundary layer, so that the tip-vortex system and near-wall shear layer occupy a larger fraction of the measurement window. As a result, the dominant vortical structures within the slipstream can be resolved with higher spatial resolution using sPIV. In this sense, the present configuration should be interpreted as a geometrically “scaled-up” version of the Phase 1 campaign, specifically designed to enable better-resolved measurements of slipstream–boundary-layer interaction.

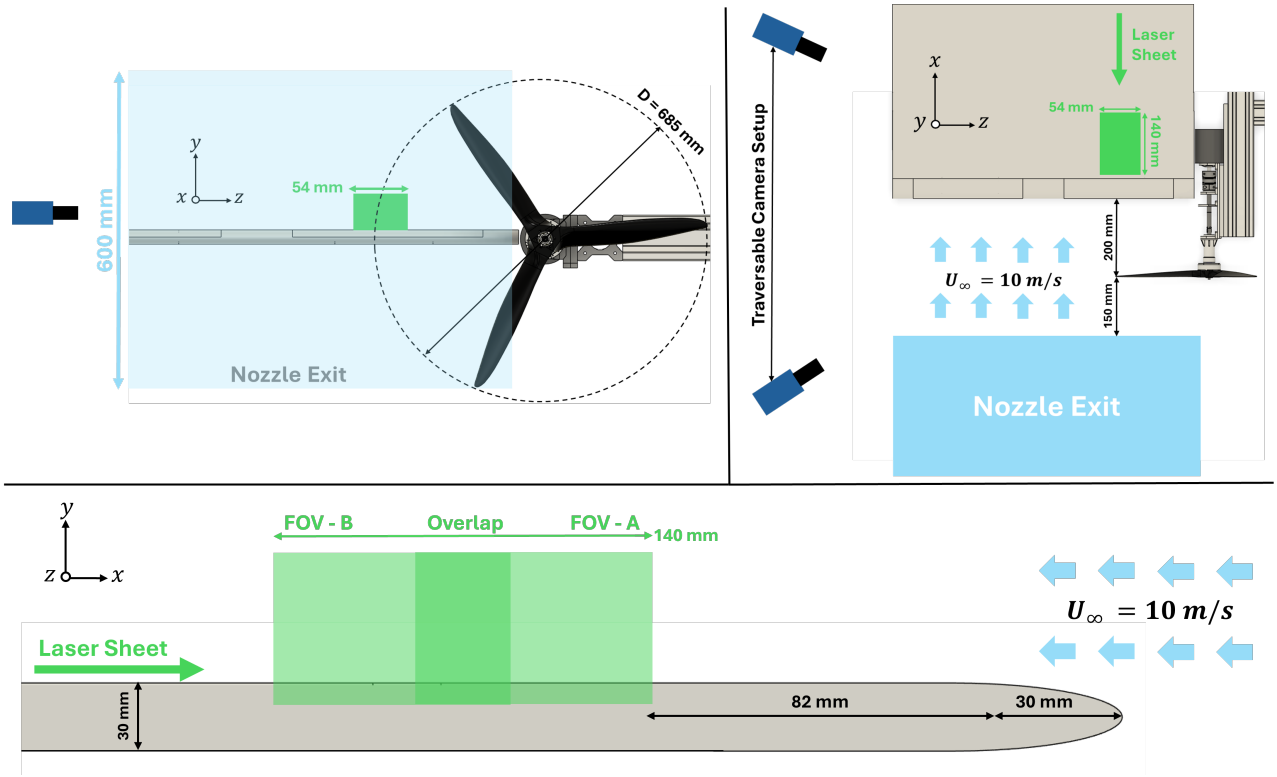

Figure 3.9: Experimental Setup Schematic. Only for illustrative purposes and not to scale.

The study captured acquired data over multiple spanwise locations with the objective of studying how the slipstream progresses both in the spanwise and chordwise direction and how it affects the downstream boundary layer. The spanwise traverse positions that were captured on the flat plate corresponded to Z/R positions inboard to outboard as shown in Table 3.1.

Table 3.1: Spanwise traverse positions of the sPIV measurement system.

Z_{rel} (mm)	$\approx Z/R$
-28	0.92
-34	0.90
-40	0.88
-46	0.87
-52	0.85
-58	0.83
-64	0.81
-70	0.80
-76	0.78
-82	0.76

3.2.2. Test Model

During this campaign, the measurements were conducted over a flat plate with a semi-elliptical leading edge located 350 mm downstream from the wind tunnel nozzle. The ellipse dimensions were chosen to promote smooth flow attachment at the leading edge while minimising the influence of leading-edge curvature on the slipstream–boundary-layer interaction. After the elliptical section ends, the plate becomes fully flat and extends 1.1 m downstream. A small flat-plate flap was

added at the trailing edge of the flat plate to vary the flow without rotating the model itself, which is significantly large. The motive behind the flap was to increase the effective camber, thereby making the streamwise pressure gradient near the leading edge more adverse when the flap is deflected, henceforth emulating an overall positive AOA deflection of the flat plate. However, preliminary tests indicated no measurable change in the leading-edge pressure gradient, most likely due to the flap's downstream location and limited chordwise extent relative to the plate. Consequently, the analyses reported here consider cases without imposed pressure-gradient modification.

The elliptical leading edge consisted of two rows of 16 pressure taps each, spaced 10 mm apart. The location of the pressure taps was chosen to align with the relative position of the propeller to the plate, allowing for the quantification of streamwise time-averaged wall pressure both inside and outside the propeller slipstream. Static pressure was recorded with a 160 Pa full-scale pressure scanner at 10 Hz for 15 s, for both propeller-on and propeller-off conditions. The pressure taps are connected to the pressure scanners using thin tubes to individual modules. Each of the modules converts air pressure into electrical voltages. These voltages are fed into the DAQ system, which digitises the voltage signals and transmits them to the PC. These signals are then converted back to pressure data, and the final output is acquired in Pascals.

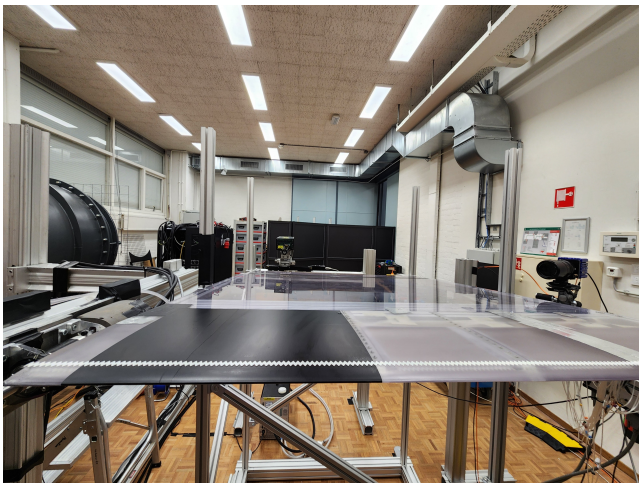

Figure 3.10: Image of the Flat Plate. Tests were conducted without the zigzag tape. Black masking is applied to prevent reflections while acquiring images for sPIV.

3.2.3. Propeller Geometry

A three-bladed carbon fibre propeller, 68.58 cm in diameter and with a fixed pitch of 34.08 cm, manufactured by Mejzlik Propellers, has been used in this campaign. The propeller drivetrain was mounted on an aluminium X-95 beam assembly so that the propeller's disk plane sat 150 mm downstream of the nozzle exit. The rotor turned anticlockwise when viewed from upstream and was oriented in the *y*–*z* plane for two reasons: (i) to maximise the portion of each blade that passes through the open-jet core as opposed to the shear layer near the nozzle exit, and (ii) to increase the time of that immersed blade segment within the angular sector above the plate. In this configuration, roughly one quarter of the disk area intersects the wind-tunnel jet.

The operating point of the propeller corresponded to a thrust coefficient (T_c) of 1, evaluated under the idealised assumption of uniform inflow across the entire disk, comparable to high-thrust take-off conditions of most modern turboprop aircraft. As there was no load cell to measure the forces on the propeller, the operating conditions were inferred from the propeller performance curves obtained from the manufacturer, resulting in a rotational speed (n) of 48.6 Hz. At a freestream velocity (U_∞) of 10 m/s, the advance ratio (J) corresponds to 0.3.

Figure 3.11: Propeller used for the PIV campaign.

3.2.4. sPIV Setup

Stereoscopic PIV is a planar, three-component velocity-measurement technique (“3C–2D”). A thin laser sheet illuminates tracer particles in a single measurement plane; two cameras view that same plane from oblique angles (typically with Scheimpflug adapters to keep the tilted image in focus). Each camera records a time-separated image pair that is processed by cross-correlation to obtain image-space particle displacements. Using a geometric calibration (mapping functions from each camera’s image to the physical plane), the two displacement fields are combined to reconstruct the full velocity vector (u, v, w) within the illuminated plane—streamwise, wall-normal and spanwise components, respectively. The accuracy of sPIV depends strongly on careful optical calibration and precise laser-sheet alignment. Since the laser sheet has a finite thickness, velocity gradients normal to the sheet are effectively smeared out, and strong out-of-plane motion can decorrelate the particle images and therefore reduce measurement accuracy.

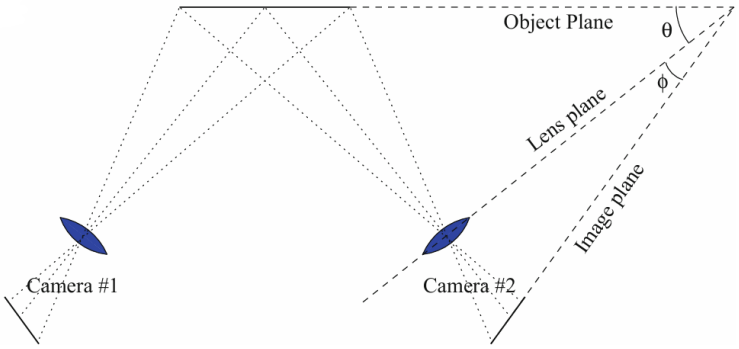

Figure 3.12: Stereoscopic imaging configuration - angular lens displacement with tilted back plane (Scheimpflug condition) [31]

The sPIV instrumentation comprised two cameras viewing a laser sheet, with each element mounted on a dedicated Zaber X-LRQ linear traverse. Motions were synchronised via external controllers, enabling precise, repeatable positioning along the spanwise coordinate z. For each field of view (FOV), measurements were acquired at ten spanwise stations separated by $\Delta z = 6\,\mathrm{mm}$. Collectively,

these stations span from just outboard of the blade tip progressively inboard towards the blade root, and were assembled to form a continuous spanwise map of the flow.

The setup used in this campaign included two 16-bit LaVision Imager sCMOS with a 2560 $\times$ 2160 px^2 sensor and a pixel size of 6.5 μm. A 200 mm lens was mounted onto each camera to allow for the required Field of View (FOV). The flow was seeded using a SAFEX Twin Fog DP generator, with a mixture of diethylene glycol and water, and was illuminated using a 200 mJ Quantel Evergreen low-speed laser.

Figure 3.13: LaVision Imager sCMOS camera.

Figure 3.14: SAFEX Fog generator.

Figure 3.15: Quantel Evergreen laser and power supply.

The system provided a field of view (FOV) of 90 mm $\times$ 54 mm for each position of the stereo-image plane. After the first set of velocity measurements, the two cameras were then moved downstream (x-direction or chordwise), and a second set of velocity measurements was acquired over an overlapping FOV of the same dimensions. This allowed for a total FOV of 140 mm $\times$ 54 mm while maintaining resolution in the wall-normal direction. After each FOV was obtained, self-calibration had to be conducted for the sPIV.

A LaVision Programmable Timing Unit (PTU) was used to synchronise the sPIV acquisition, generating all triggers for the dual-frame cameras and the dual-cavity laser (Q-switch and flashlamp lines). For phase-locked measurements, the PTU was synchronised to the propeller encoder's once-per-revolution (1P) signal, which defined the azimuthal origin ($\phi = 0°$). Following each 1P pulse, the PTU applied a programmable delay

$$t_\phi = \frac{\phi}{360°} T_{\mathrm{rev}} = \frac{\phi}{360° \, f_{\mathrm{rev}}},$$

where $T_{\mathrm{rev}} = 1/f_{\mathrm{rev}}$ is the instantaneous rotational period computed from the encoder. At $t = t_\phi$, the PTU issued the precisely timed sequence to (i) expose frame A on the cameras, (ii) fire laser pulse A, (iii) wait the inter-frame time Δt chosen from the expected in-plane displacement to remain within the sPIV dynamic range, (iv) expose frame B, and (v) fire laser pulse B. This ensured that each vector field corresponded to the same blade azimuth at the target phases $\phi = 60°$, $100°$ and $140°$.

A stroboscope was used to establish and verify the phase reference prior to acquisition.The strobe was electronically linked to the ESC so that its flash frequency followed the actual rotational speed of the propeller. With the motor running, a small reference mark on the hub was aligned with a fixed mark on the nacelle, and the strobe phase was adjusted until this mark appeared stationary; this position was taken as $\phi = 0°$. Once this reference had been set, the PTU phase delays corresponding to $\phi = 60°, 100°$ and $140°$ were prescribed were prescribed using the encoder's 1P signal. The propeller was removed while setting up the phase-locking system due to safety concerns.

500 image pairs were acquired for the clean (propeller-off) and each phase-locked propeller-on cases. For the time-averaged propeller-on cases, the image pairs were randomly acquired at a fixed acquisition frequency of 15 Hz. 1000 image pairs were acquired in the time-averaged cases to improve convergence of the mean and flow statistics.

3.2.5. Tunnel Operating Conditions

The tunnel was operated at a freestream velocity $U_\infty = 10\,\mathrm{m\,s^{-1}}$, set by the structural and power limits of the propeller system. The Reynolds number based on the local boundary-layer thickness, Re_δ, varied with chordwise position between 2.8×10^3 and 4.5×10^3. Here, δ denotes the nominal boundary-layer thickness defined by the δ_{99} criterion. In this context, using Re_δ is appropriate because the relevant dynamics are governed by the boundary layer itself and using Re_δ therefore provides a more appropriate scaling for the slipstream–boundary-layer interaction and facilitates comparison with full-scale conditions. The propeller was operated at a single advance ratio of 0.3 which corresponded to a rotational speed of 48.6 Hz.

4

Results and Discussion

This chapter presents the results of the two experimental campaigns and discusses the corresponding interpretations. In section 4.1, the results from the Phase 1 campaign based on oil-flow visualisation and acoustic measurements are presented, followed by section 4.2, which reports the stereoscopic PIV results from the Phase 2 campaign.

4.1. Phase 1 - SES and OFV Measurements

In this section, the results from the first experiment described in section 3.1 will be discussed, where the effect of the slipstream on the wing boundary layer was studied. The rotational axis of the propeller was kept parallel to the freestream flow, and the wind tunnel was operated at a speed of 20 m/s. The objective of the experiment was to understand the flow characteristics of the boundary layer under the influence of the propeller slipstream in a take-off or landing configuration, and as such, focuses on high angle-of-attack cases. Comparisons have been done using acoustic data and OFVs across different cases.

The arrangement of the microphones and pressure sensors embedded in the SES is shown in Figure 4.1. All results presented in this chapter follow the numbering and convention defined in this figure. For clarity, the microphones will hereafter be referred to as belonging to the *first*, *second*, or *third* row, depending on their spanwise placement.

The chordwise positions of the microphones, expressed in terms of x/c, are defined relative to the airfoil geometry. These positions are not identical on the suction and pressure sides, reflecting the specific layout of the SES. The corresponding locations are summarised in Table 4.1.

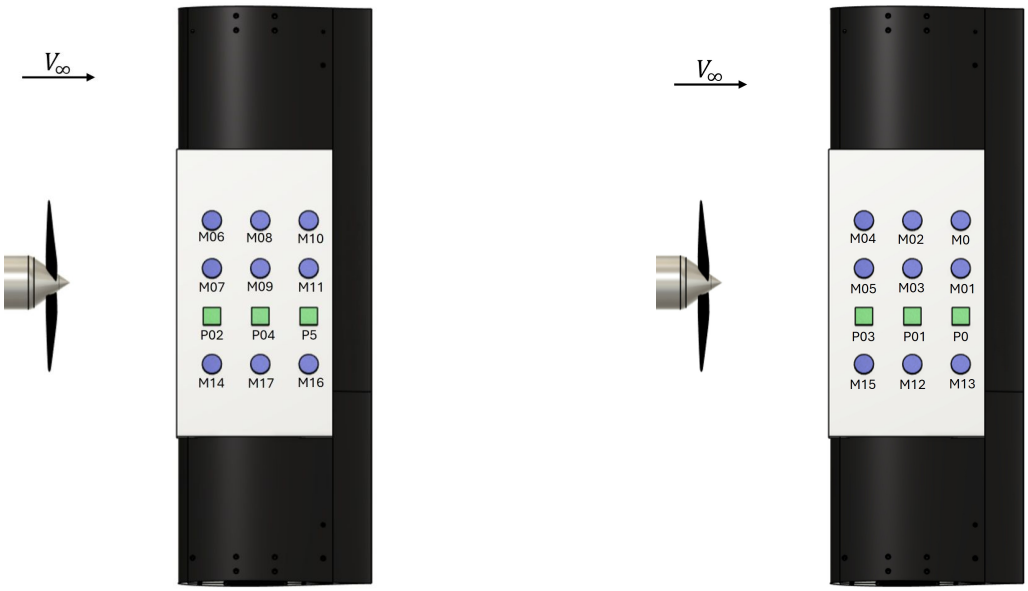

(a) Suction side of the setup.

(b) Pressure side of the setup.

Figure 4.1: Schematic of the SES wrapped around the airfoil, showing the arrangement of microphone and pressure sensor channel numbers. The layout reflects the actual physical configuration of the SES. Illustration is not to scale.

Surface	Microphones	Pressure Sensors	Chordwise Location (x/c)
Suction Side	6, 7, 14	2	0.165
	8, 9, 17	4	0.370
	10, 11, 16	5	0.620
Pressure Side	4, 5, 15	3	0.125
	2, 3, 12	1	0.325
	0, 1, 13	0	0.565

Table 4.1: Microphone and pressure sensor layout with chordwise locations.

4.1.1. Interpretation of Microphone Data

Following the post-processing of the raw microphone data by adjusting for gain and background noise, the Sound Pressure Levels (SPL) were determined across each microphone for each test case and were compiled into a contour plot, such as the one shown in Figure 4.2. The microphone positions have been marked to indicate the spatial resolution of the data that is available. It is important to note that, based on the position of the SES on the airfoil, there is no data available to the left of the 0.165 x/c chord location of the airfoil.

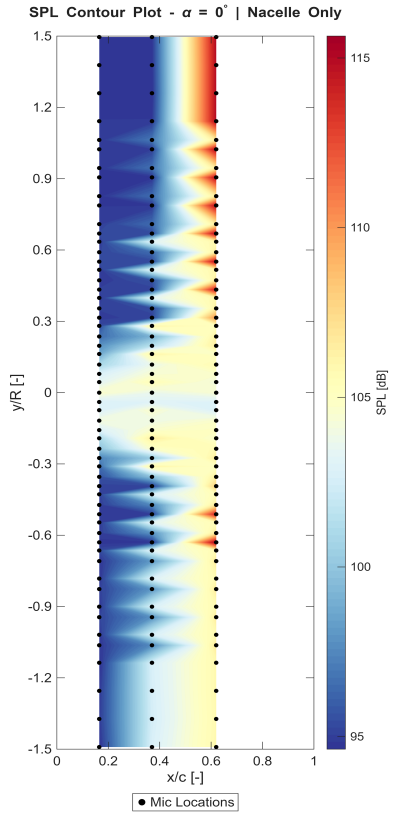

Figure 4.2: SPL contour plot for the nacelle only case at $\alpha = 0°$.

It is important to clarify what the contour maps do and do not represent. Each microphone provides a point measurement of SPL at its corresponding x/c and y/R location, and the values obtained from in between the microphones have been linearly interpolated. The plotted field is created either by the contouring routine's internal piece-wise linear interpolation on the measured grid, or by an explicit 2-D interpolation. These intermediate values are therefore estimates calculated from neighbouring microphones, not additional measurements. The measured microphone positions are marked on the figure to make this distinction explicit and to indicate the available spatial resolution.

For the propeller-on cases, the positive y/R values represent the upgoing blade side of the propeller while negative y/R values represent the downgoing blade side. To keep a consistent sign convention and for easier comparison, the same sign convention has been used for the propeller-off (nacelle only) cases as well.

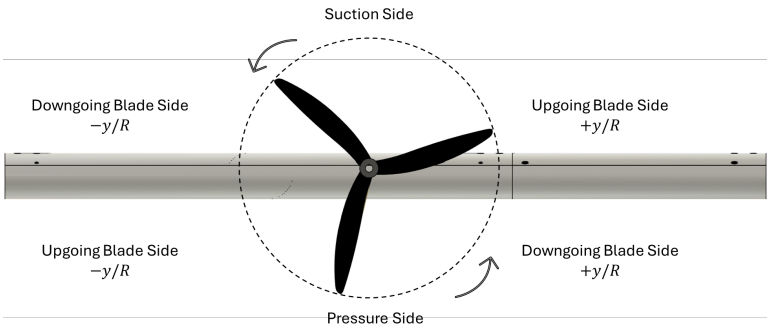

Figure 4.3: Sign conventions for upgoing and downgoing blade side. The arrow denotes the direction of propeller rotation.

4.1.2. Investigation of Discontinuities in Microphone Data

Upon a closer examination of Figure 4.2, a lot of discontinuities appearing as streaks can be observed. Preliminary inferences suggested that these were an artefact of the interpolation functions used and that incorrect data processing caused these streaks to appear. These streaks were consistently observed in all the test cases, which involved variations in the advance ratio (J) as well as the angle of attack.

In order to determine whether these streaks were solely because of data processing or whether they appeared due to some kind of fluctuation in the flow field, the SPL values of each microphone were plotted individually as shown in Figure 4.4. Here, it can be observed that the contours change relatively smoothly as compared to Figure 4.2, leading to the conclusion that there is some kind of physical phenomenon causing large fluctuations in the SPL values in the second and third row of microphones. The SPL values much higher than expected in the second and third row of microphones, especially for a propeller-off case at 0° AOA where the pressure gradient is mostly favourable. The OFV plot of the nacelle only case (Figure 4.7a) is a direct representation of what is happening in the flow field and can therefore be used to understand the acoustic measurements better.

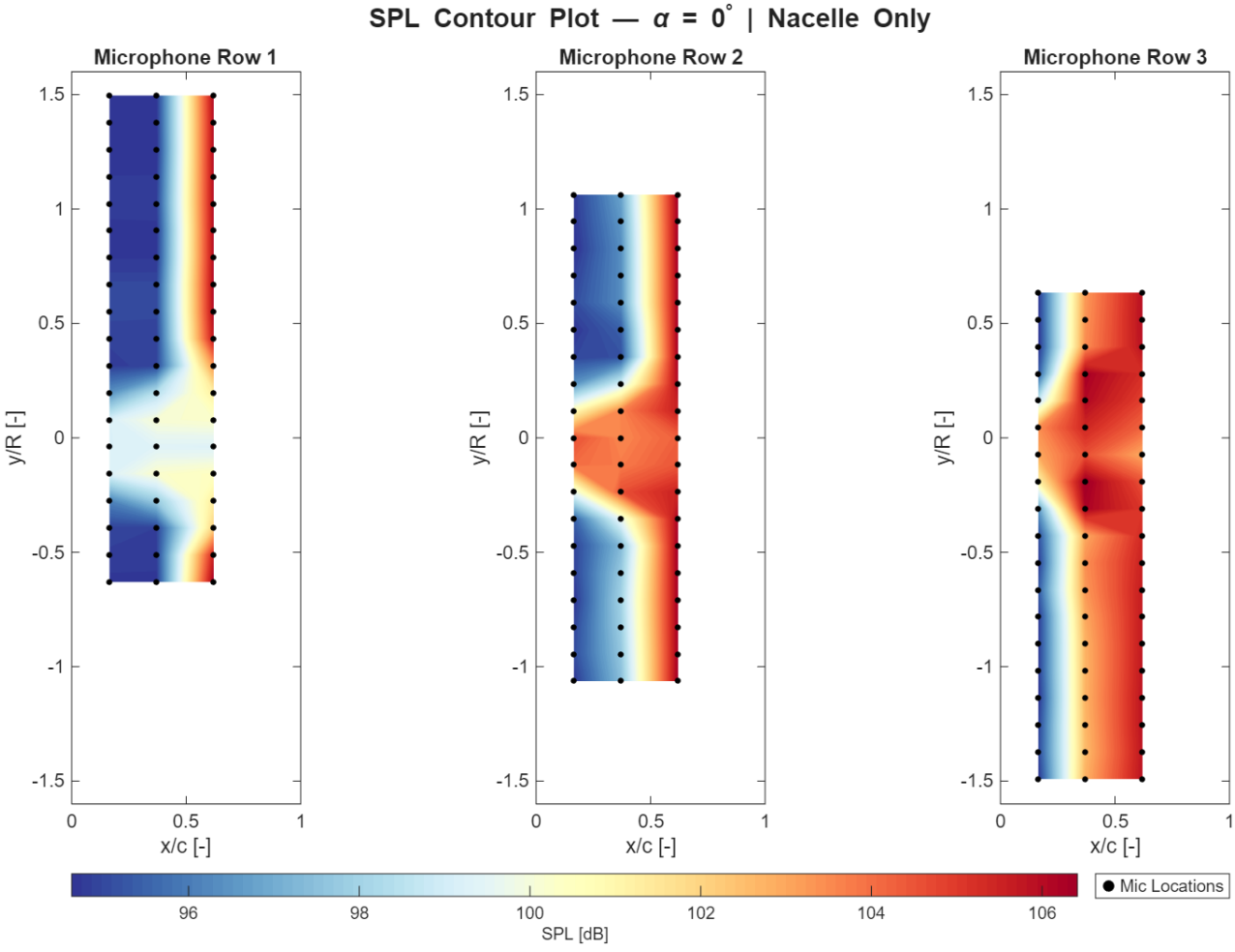

Figure 4.4: Row-wise SPL contour plots for the nacelle only case at $\alpha = 0^\circ$.

In Figure 4.5, it can be observed that there within the region of the SES, there exists the onset and the region of a LSB. However, since this is a nacelle only case, the LSB exists for the entire spanwise

region so there should not be any reason as to why only the second and third row of microphones in Figure 4.4 record higher SPL values as compared to the first row of microphones.

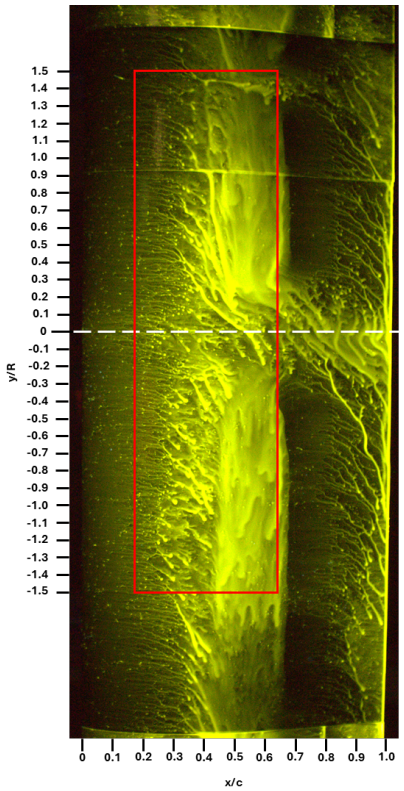

Figure 4.5: OFV for the nacelle only case at $\alpha = 0^{\circ}$. The white dotted line represents the region where the hub of the propeller is located. The red rectangle approximately represents where the SES was placed.

In order to understand the inconsistencies better, the Power Spectral Density (PSD) plots were plotted for the three microphone rows. It can clearly be observed that Mics 9 and 17 record much higher broadband energy as compared to Mic 8. These high energy levels are similar to what is typically observed in adverse pressure gradients. On the other hand, Mic 8 records lower broadband energy levels akin to that of a relatively favourable pressure gradient, consistent with what could potentially be observed in the case of an airfoil with no deflection.

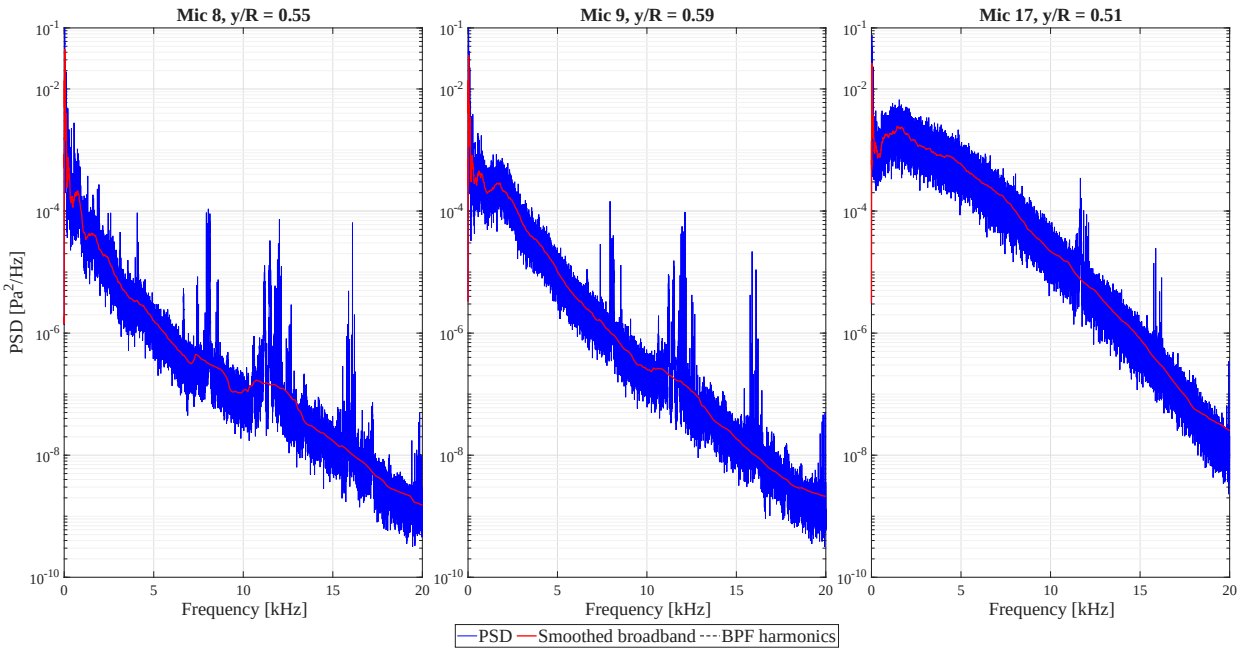

Figure 4.6: PSD of the propeller off case in the suction side at $\alpha = 0°$. All three spectral plots are from the mics located at 0.37 x/c of the airfoil taken at relatively the same spanwise locations. BPF harmonics are not applicable for this case. Mics 8, 9 and 17 corresponds to the first, second and third row of microphones.

There also exist multiple tonal spikes which can be attributed to the existence of the LSB. Tonal spikes observed during the onset of a LSB arise from the instability of the separated shear layer. When the laminar boundary layer separates, the velocity profile over the bubble becomes strongly inflectional and highly susceptible to Kelvin–Helmholtz (K–H) instabilities. Disturbances at a preferred frequency are selectively amplified as they convect downstream, rolling up into coherent vortices in the separated shear layer. As these vortices impinge on the reattachment region and the trailing edge, they are efficiently scattered into acoustic waves, producing narrowband tones in the pressure spectra. The result is a series of pronounced tonal peaks superimposed on the underlying broadband turbulence associated with the bubble.

A possible explanation for the erroneous data is that the row of pressure sensors that exists between the second and third row of microphones protrudes out of the SES, causing local flow disturbances. A chordwise line of slightly protruding pressure sensors located between the second and third microphone rows behaves as a weak roughness fence. It locally energises the boundary layer, causing micro-separation or transition, increasing near-wall broadband pressure fluctuations, and scatters the incident acoustic field. Microphones immediately adjacent to the fence therefore measure the superposition of the incident and scattered fields, yielding spanwise SPL offsets relative to the first row. All subsequent analyses will only include the first row of microphones for an accurate representation of the flow field.

4.1.3. Analysis of the Nacelle Only Cases

This subsection compares the flow characteristics between the nacelle-only cases at angles of attack $0°\alpha$, $9°\alpha$ and $12°\alpha$. The formation of an LSB was observed as the experiment was conducted in a low Reynolds number, consistent with previous experimental studies [32]. The presence of an LSB will also affect flow characteristics within the slipstream when the propeller is turned on which will be discussed in subsection 4.1.4.

4.1.3.1. Oil Flow Visualisations (OFVs)

Figure 4.7 presents the OFVs for the propeller-off cases, with the main regions of interest annotated and described in the figure caption. The corresponding flow features are discussed in the following paragraphs.

As the AOA increases, there is an increase in the adverse pressure gradient, causing two main effects: (1) The LSB moves upstream of the airfoil; (2) Flow separation occurs earlier on the airfoil. These two distinct effects can be observed in OFVs in Figure 4.7.

The location of the LSB moves upstream with an increase in angle of attack. At $0°\alpha$ (Figure 4.7a), the LSB is visible between 0.3 and 0.6 x/c followed by turbulent reattachment. At both $9°\alpha$ (Figure 4.7b) and $12°\alpha$ (Figure 4.7c), the LSB moves to the leading edge of the airfoil.

At $0°\alpha$, the pressure gradient remains fairly favourable, so the flow never separates over the airfoil. At $9°\alpha$, flow separation occurs at approximately 0.7 x/c while at $12°\alpha$, separation occurs at approximately 0.55 x/c.

Another observation is the effect of the nacelle wake on the airfoil. At 0 y/R, where the nacelle is present, there appears to be a slight recirculation of the flow, characterised by a hump like structure at the separation line of the $9°\alpha$ and $12°\alpha$ cases.

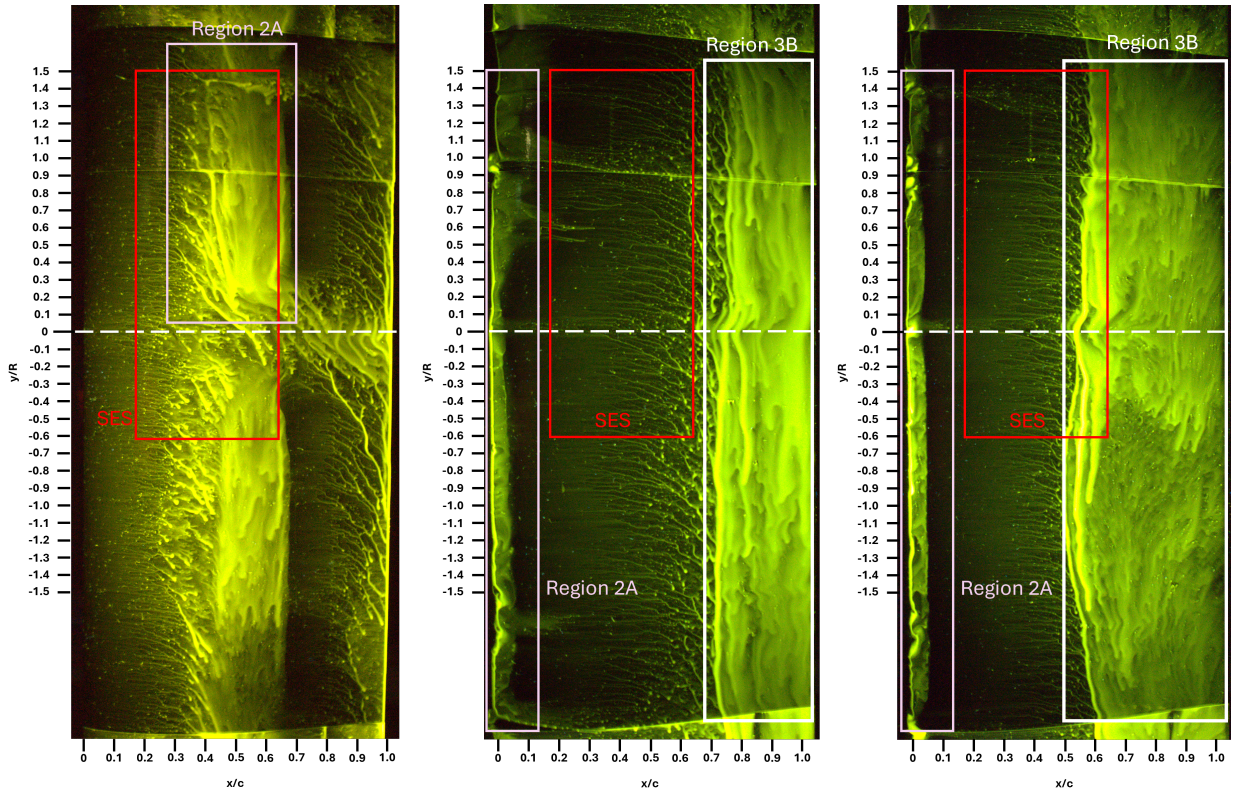

(a) $\alpha = 0°$. **(b)** $\alpha = 9°$. **(c)** $\alpha = 12°$.

Figure 4.7: OFV of the nacelle only cases in the suction side. The white-dashed line represents the wake of the nacelle. The red rectangle represents the SES. Region 2A represents the LSB. Region 3B represents the separation region on the airfoil.

When a laminar separation bubble (LSB) is present, its signature can be clearly identified in oil-flow visualisations. The onset of separation produces distinct separation streamlines and shear lines, while the reattachment downstream of the bubble is marked by the convergence of oil streaks.

A characteristic feature of LSBs in oil-flow images is the accumulation of oil just upstream of the separation line. This occurs because the separated airflow can leave the surface region, whereas the oil cannot be ejected with it. Instead, the shear forces transport the oil toward the separation location, where it accumulates into a thickened, dark region. In many cases, this appears as a “bump” or black patch in the oil-flow image. Once sufficient oil builds up in this region, gravity causes it to drain away from the separation line, leaving streaks that mark the stagnation or separation streamline. These patterns provide a reliable indirect indication of the presence and extent of an LSB.

4.1.3.2. Acoustic Measurements - Comparison of SPL Plots

Figure 4.8 illustrates the SPL levels across the top row of microphones across different angles of attack. As explained in subsection 4.1.2, the focus is only on the top row of microphones. The SPL contour plots can be comparable to the OFVs in Figure 4.7. It is important to note that the sound pressure level (SPL) does not represent a truly steady quantity. SPL is derived from the unsteady pressure fluctuations recorded by the microphones and is defined as a logarithmic measure of the Root-Mean-Square (RMS) pressure relative to a reference level. In other words, while the underlying acoustic field is inherently unsteady in time, the SPL provides a statistical representation of its average intensity. Consequently, the SPL contour plots presented in this work should be interpreted as averaged measures of the unsteady acoustic response, rather than as time-resolved flow phenomena.

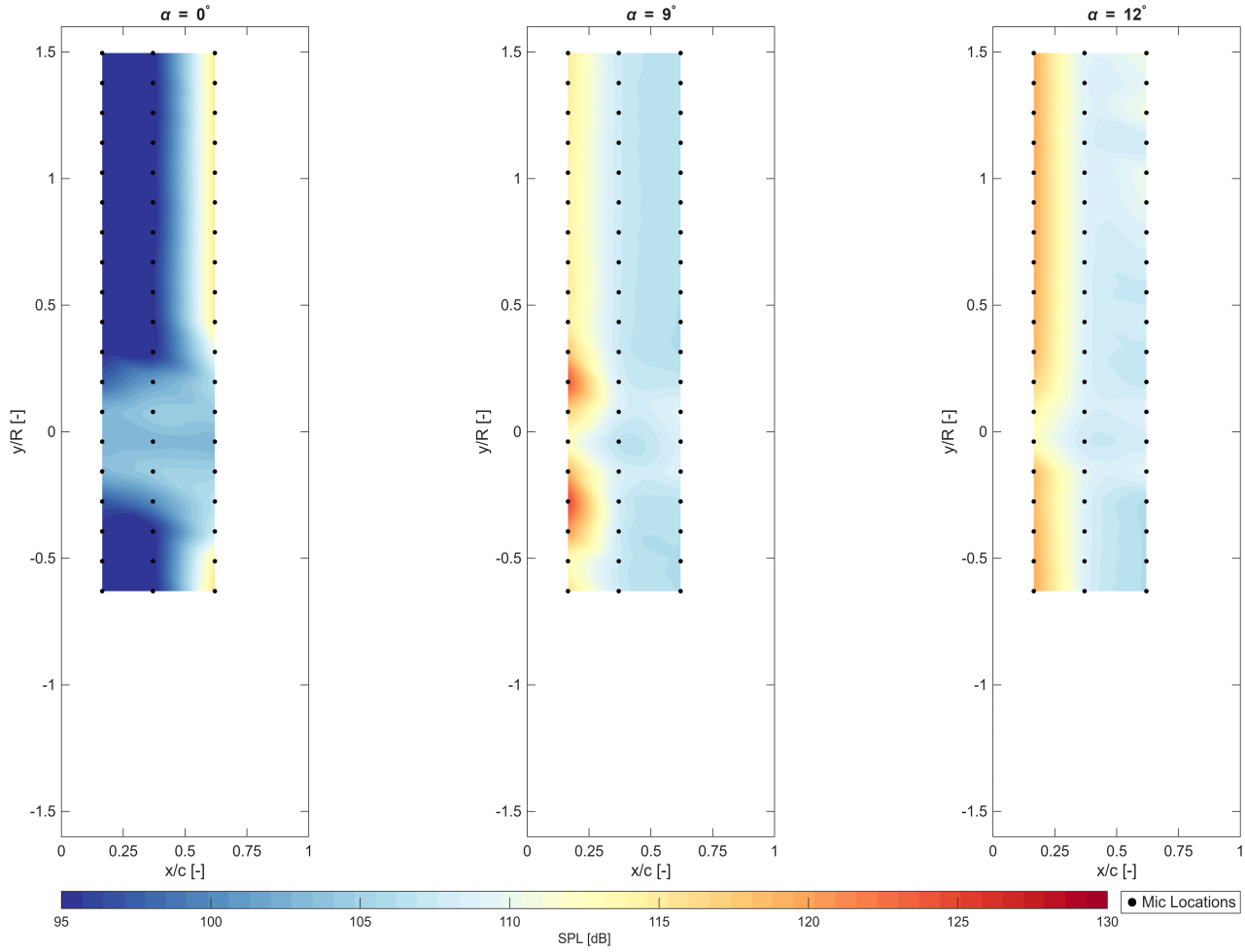

Figure 4.8: SPL of the nacelle only cases in the suction side at $\alpha = 0°, 9°,$ and$12°$. The domain is limited to $0.16 \leq x/c \leq 0.62$.

Across the three AOAs, an increase in SPL levels can be observed at 0 y/R. This is representative of the nacelle wake. From the OFVs, it is known that there exists an LSB in the 0° case between approximately 0.37 x/c and 0.62 x/c. This can be visualised in the SPL plot (Figure 4.8) as well, where the microphones at 0.62 x/c record a peak in the SPL values, indicative of turbulent reattachment of the flow. However, due to a more favourable pressure gradient as compared to the higher AOA cases, the overall SPL level in the 0° case remains lower as compared to the 9° and 12° cases.

Followed by turbulent reattachment at the end of the LSB located at the leading edge of the higher AOA cases, the first column of microphones (0.16 x/c) records every high SPL value. Further downstream, the SPL reduces as the flow approaches separation. This occurs because turbulent but attached flow on an airfoil produces higher surface SPL than separated flow, as the energetic turbulent boundary layer interacts more strongly with the airfoil surface and trailing edge. Separated flow, while featuring large-scale structures, results in lower broadband SPL at the surface microphones [33].

4.1.4. Analysis of the Propeller On Cases

The propeller-off results presented in subsection 4.1.4 provide a reference baseline for interpreting the propeller-on cases discussed here. This section compares the flow characteristics between the propeller-on cases at angles of attack $0^\circ\alpha$, $9^\circ\alpha$ and $12^\circ\alpha$. The propeller was being operated at an advance ratio of 0.8 and at a rotational speed of 123 RPS.

4.1.4.1. Oil Flow Visualisations

Figure 4.9 presents the oil-flow visualisations (OFVs) for the propeller-on cases, with the main regions of interest annotated and described in the figure caption. The corresponding flow features are discussed in the following paragraphs.

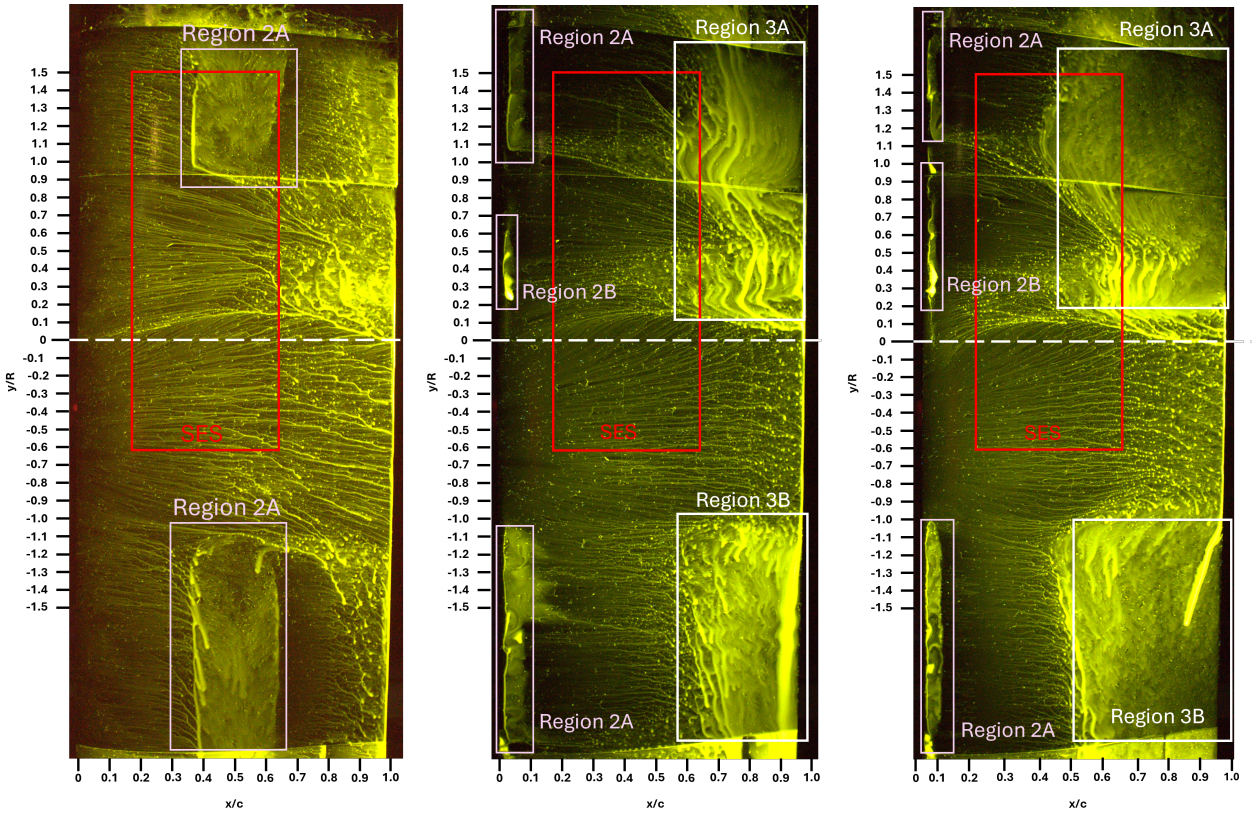

(a) $\alpha = 0°$. **(b)** $\alpha = 9°$. **(c)** $\alpha = 12°$.

Figure 4.9: OFV of the propeller on cases in the suction side. The white-dashed line represents the centre of the nacelle hub located upstream of the airfoil. The red rectangle is the region where the SES was placed. Region 2A and 2B represent the LSB outside and inside the slipstream, respectively. Region 3A and 3B represent the separation region on the upgoing blade side and downgoing blade side, respectively.

On the upgoing blade side, the local swirl induced by the propeller increases the effective angle of attack of the incoming flow. As a result, the suction-side pressure becomes more negative, leading to a higher local lift and causing the streamlines to contract and converge along the chordwise direction. Conversely, in the downgoing blade side, the induced velocity reduces the effective angle of attack, producing a weaker suction effect and a divergence of streamlines along the chordwise direction. This behaviour is consistently observed across all three angles of attack shown in Figure 4.9.

Outside the propeller slipstream, the LSB (Region 2A in Figure 4.9) forms at 0.4 x/c in the $0°$ AOA followed by reattachment at approximately 0.65 x/c. At the $9°$ and $12°$ AOAs, the LSB forms at the leading edge of the airfoil. The shift of the LSB further upstream is characterised by the presence of a stronger adverse pressure gradient with an increase in the AOA, which causes earlier boundary layer separation and transition to turbulence. Furthermore, the length of the LSB becomes shorter as turbulent reattachment occurs sooner. This phenomena has been well-documented in previous studies by Singh et. al [34].

Flow separation can be observed in the $9°$ and $12°$ cases highlighted by region 3A and 3B. As expected, the separation region moves further upstream with the increase in angle of attack. from At $0°$ AOA, the pressure gradient is not adverse enough so there is no flow separation that can be observed. Interestingly, at the higher angles of attack, the separation region seems to exhibit recirculation behaviour which was not observed in the nacelle-only cases from Figure 4.7. This suggests that the propeller slipstream induces increased momentum in the flow complemented

by the vortex interactions which modify the boundary layer dynamics in the separated region. The slipstream energizes the boundary layer and modifies separation, but the strong adverse pressure gradient and induced vortices sustain or reshape recirculation zones, making the flow highly unsteady and complex. Furthermore, within the propeller slipstream, the high momentum flow also energises the boundary layer which seems to delay flow separation compared to outside the propeller slipstream.

Another observation is that in the downgoing side of the propeller, no flow separation occurs even at higher AOAs even though the phenomena can be observed in the upgoing blade side of the propeller and the nacelle-only cases (Figure 4.7). The most likely reason for this is a combination of Reynolds effects and a decrease in the effective AOA due to a negative swirl induced by the propeller on the downgoing blade side. The slipstream causes the local flow velocity to increase causing an increase in the Reynolds number due to which, the flow may have potentially transitioned at the leading edge of the airfoil and is fully turbulent on the downgoing side. Since the flow is turbulent, flow separation is delayed which is why it cannot be observed. Moreover, due to the decrease in the local AOA, the pressure gradient is not as adverse and the flow remains attached for the entire chordwise length of the airfoil. In order to verify the state of the flow, the PSD plots can be compared for the three AOAs in the downgoing blade side.

The laminar separation bubble can be observed only at higher AOAs and seems to be suppressed at 0° AOA. However, at higher angles of attack, the LSB forms within the propeller slipstream at the leading edge in the upgoing blade side (Region 2B in Figure 4.9b and Figure 4.9c). Furthermore, at 12° AOA, the length of the bubble extends from approximately 0.2 x/c to the blade tip as opposed to the 9° case, where the bubble ends at approximately 0.6 x/c.

From a broader perspective, the propeller slipstream introduces periodic and high-energy disturbances into the boundary layer, causing it to develop turbulent-like characteristics. This increases the momentum of the flow near the surface of the airfoil in order to keep the flow attached, thereby suppressing LSBs [24]. At higher angles of attack, the adverse pressure gradient at the leading edge becomes stronger, promoting the formation of an LSB, even in the presence of slipstream-induced turbulence. As the AOA increases from 9° to 12°, combined with the increase in effective local AOA due to the upgoing blade side of the propeller, the pressure gradient becomes more adverse, causing earlier separation and potentially allowing the bubble to grow [35].

4.1.4.2. Acoustic Measurements - Comparison of SPL Plots

Figure 4.10 represents the SPL levels across the top row of microphones across the different angles of attack when the propeller is switched on and the wing is under the influence of the slipstream. Across all three cases in the upgoing blade side, it can be observed that there is a strong increase in SPL at approximately $y/R = 0.9$ due to the trace of the tip vortex convecting downstream of the wing. The tip vortex is strongest at the edge of the slipstream, so higher SPL values can be observed at the location of the trace of the tip vortex. Outside the slipstream, there is a decrease in SPL levels due to the decrease in local flow velocity. These effects are consistent with earlier work done by Sparks et al [36].

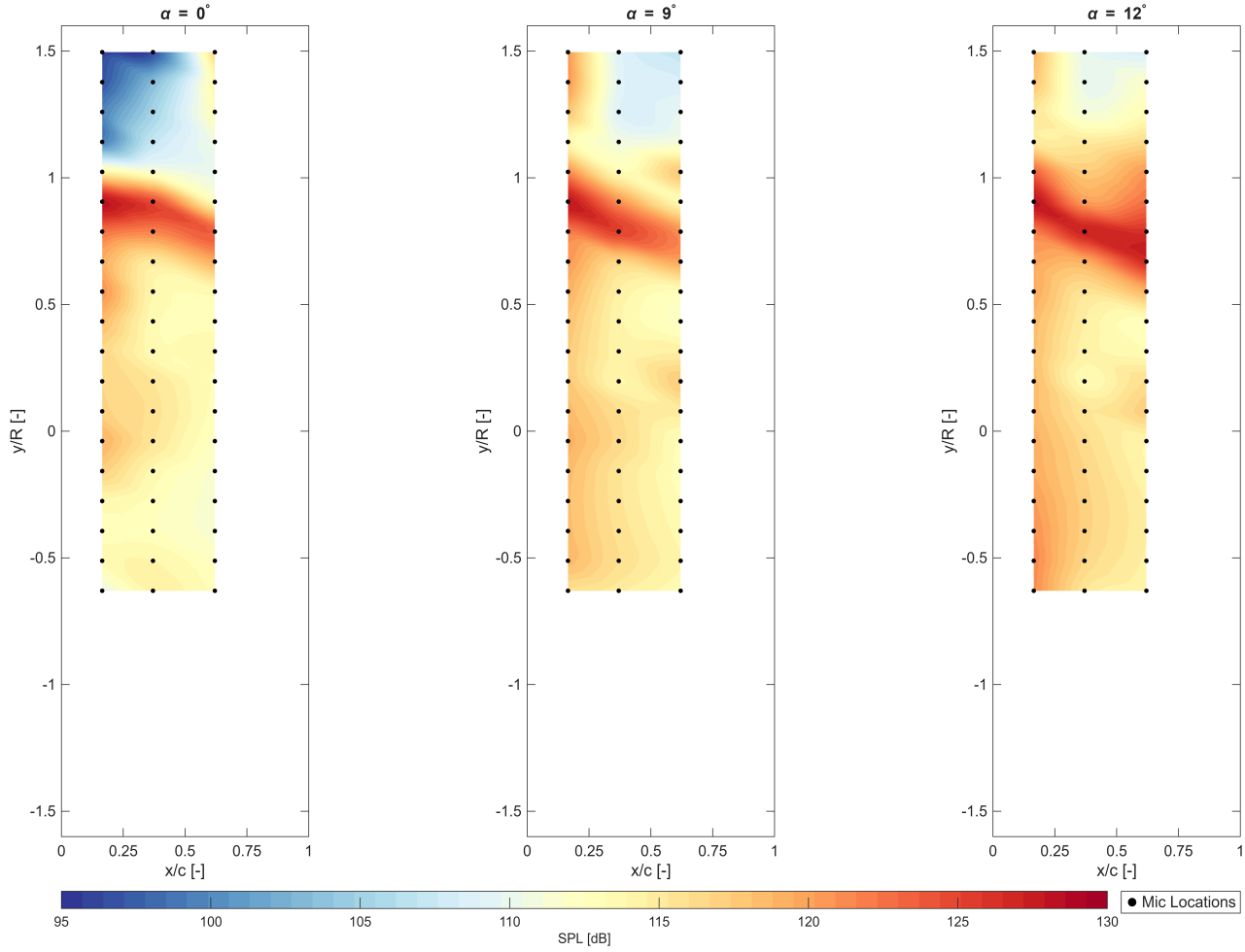

Figure 4.10: SPL of the propeller on cases in the suction side at $\alpha = 0°, 9°$, and $12°$.

The manner in which the tip vortex converges from y/R varies widely across the three cases and is very evident from Figure 4.10. When compared to the OFVs in Figure 4.9, the shape of the tip vortex region is consistent with the streamlines that were observed previously. Due to the increase in the adverse pressure gradient, the streamlines on the upgoing blade side converge further upstream as the AOA increases. The increasing adverse pressure gradient also explains why the SPL levels increase drastically outside the slipstream for the $9°$ and $12°$ cases as compared to the $0°$ case.

Based on the OFV, in the $0°$ case, an LSB forms at approximately 0.4 x/c outside the propeller slipstream. Typically, the formation of an LSB is characterised by an increase in SPL levels due to increased flow instabilities and vortex shedding. However, due to the low AOA, the overall pressure gradient is more favourable compared to the high AOA cases, thereby showcasing a relatively lower SPL level.

Outside the propeller slipstream, the SES captures the flow separation, characterised by an increase in SPL, at approximately 0.6 x/c in the $9°$ case, which increases further in the $12°$ case. Within the propeller slipstream, as expected, there is a general increase in SPL, which increases with increasing AOA.

4.1.4.3. Acoustic Measurements - Comparison of PSD Plots

Having discussed the overall spatial variations of SPL across the airfoil, it is now useful to examine the spectral characteristics of the acoustics in greater detail to identify the state of the boundary

layer. To this end, PSD plots are presented to provide a frequency domain representation of the measured pressure fluctuations. Unlike the broadband SPL distributions, which indicate the total acoustic energy within a given bandwidth, the PSD plots reveal how this energy is distributed across frequencies. This enables the identification of dominant tonal components, such as the Blade-Passing Frequency (BPF) and its harmonics, as well as broadband contributions linked to turbulent flow structures and other unsteady aerodynamic phenomena. Through this spectral analysis, a clearer understanding of the underlying flow behaviour, such as vortex shedding, boundary-layer interactions, and propeller–wake dynamics, can be obtained. Figure 4.11, Figure 4.12, and Figure 4.13 show the PSD across three different regions - outside the slipstream ($y/R = 1.37$), at the tip vortex ($y/R = 0.9$) and within the slipstream ($y/R = 0.55$). The corresponding y/R can be linked to the SPL plots shown previously.

At $\alpha = 0°$, as expected, the region outside the slipstream has relatively lower broadband energy as compared to the regions within the slipstream, indicating laminar-like characteristics. Some tonal spikes can be observed, which are most likely due to the viscous mixing of the propeller slipstream with the boundary layer outside the tip vortex. At the tip vortex, there are noticeable tonal peaks at the BPF and its harmonics as well as higher broadband levels due to the trace of the tip vortex. Within the slipstream, the broadband energy is higher as compared to outside the slipstream corresponding to what is observed in turbulent flow, but there is also a noticeable hump like structure along the frequency domain. The hump is best explained by the presence of a potentially turbulent inflow due to the propeller slipstream interacting with the airfoil as was previously observed by Wang et. al [37].

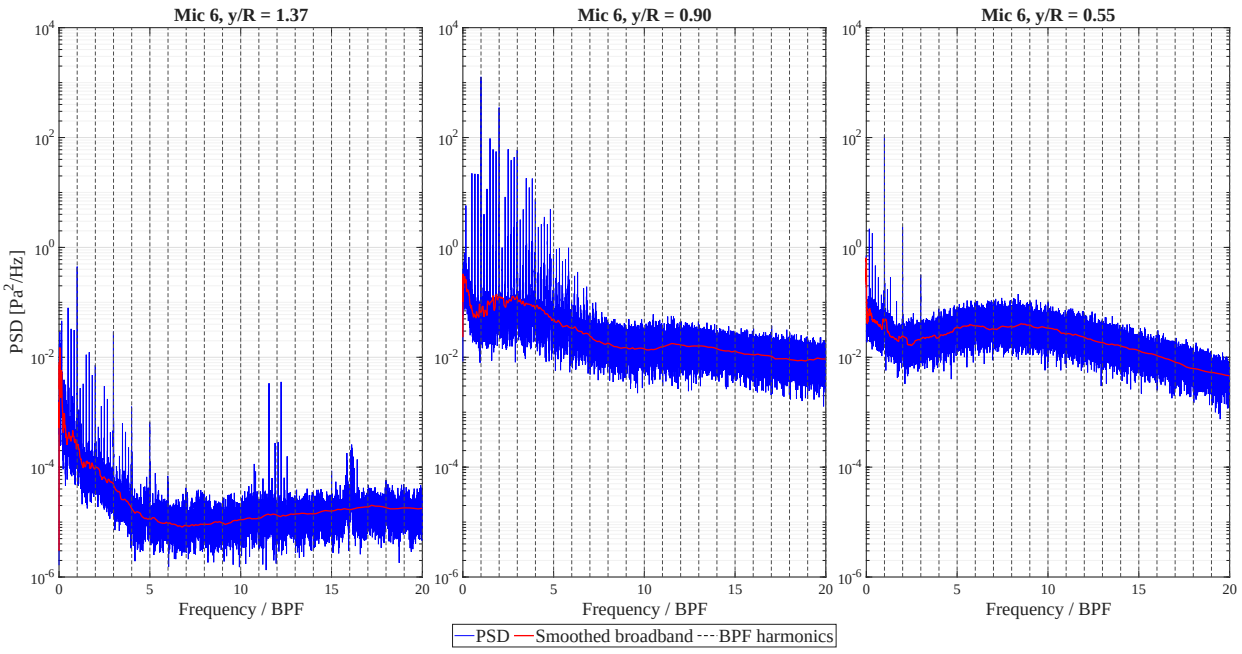

Figure 4.11: PSD of the propeller on case in the suction side at $\alpha = 0°$. The frequency has been normalised to the BPF. All three spectral plots are from the mics located at 0.2 x/c of the airfoil. 1.37 y/R represents the region outside the slipstream; 0.9 y/R represents the tip vortex region; and 0.55 y/R represents the region within the slipstream.

Compared to the $\alpha = 0°$ case, the $\alpha = 9°$ case exhibits a much higher broadband energy level outside the slipstream and at the tip vortex. This is primarily because at a higher angle of attack, there is a much higher adverse pressure gradient, causing the broadband energy levels to increase consequently. The higher broadband fluctuations outside the slipstream and at the tip vortex are also indicative of a more turbulent flow as compared to the $0°$ case. At the tip vortex, the tonal peaks are also of much higher energy as compared to the earlier case. The broadband hump, however, only

appears outside the slipstream for this AOA and not within the slipstream as was observed in the $0°$ case. A potential reason for this is that from the OFV, it was evident that there is a formation of an LSB at the leading edge of the airfoil, followed by reattachment. The flow reattaches before reaching the microphone location but after reattachment, the boundary layer is turbulent, which tends to produce a more uniform broadband noise spectrum without a pronounced hump as observed previously [38]. At $0°$, there is no LSB present within the propeller slipstream, causing the boundary layer to remain laminar or transitional over a longer chordwise extent, making it more susceptible to instability waves or direct interaction with turbulent inflow, causing it to generate a more distinct spectral hump [39].

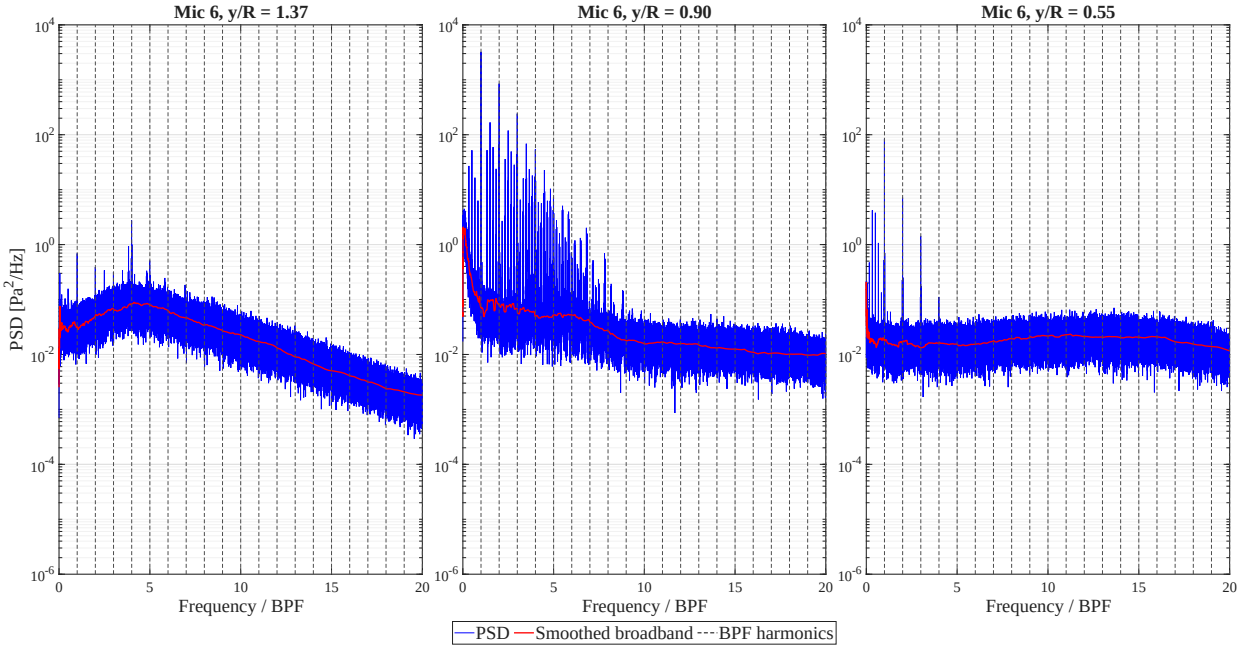

Figure 4.12: PSD of the propeller on case in the suction side at $\alpha = 9°$.

While one would expect higher broadband fluctuations and greater tonal peaks in the $12°$ case as compared to the $9°$ case due to the increasing adverse pressure gradient, the fluctuations are relatively lower for this case. Although oil-flow visualisation indicates that the LSB is longer at an AOA of $12°$ than $9°$, the measured broadband pressure fluctuations are consistently higher at $9°$.

At an AOA of $9°$, the intermediate length of the LSB suggests that it is more susceptible to Kelvin-Helmholtz (K-H) instabilities as compared to the longer LSB at $12°$. These mechanisms disrupt the coherence of shear-layer roll-up and reduce the efficiency of instability amplification. The bubble's breathing motion also becomes less energetic or more irregular, which further diminishes the overall broadband fluctuation level [40].

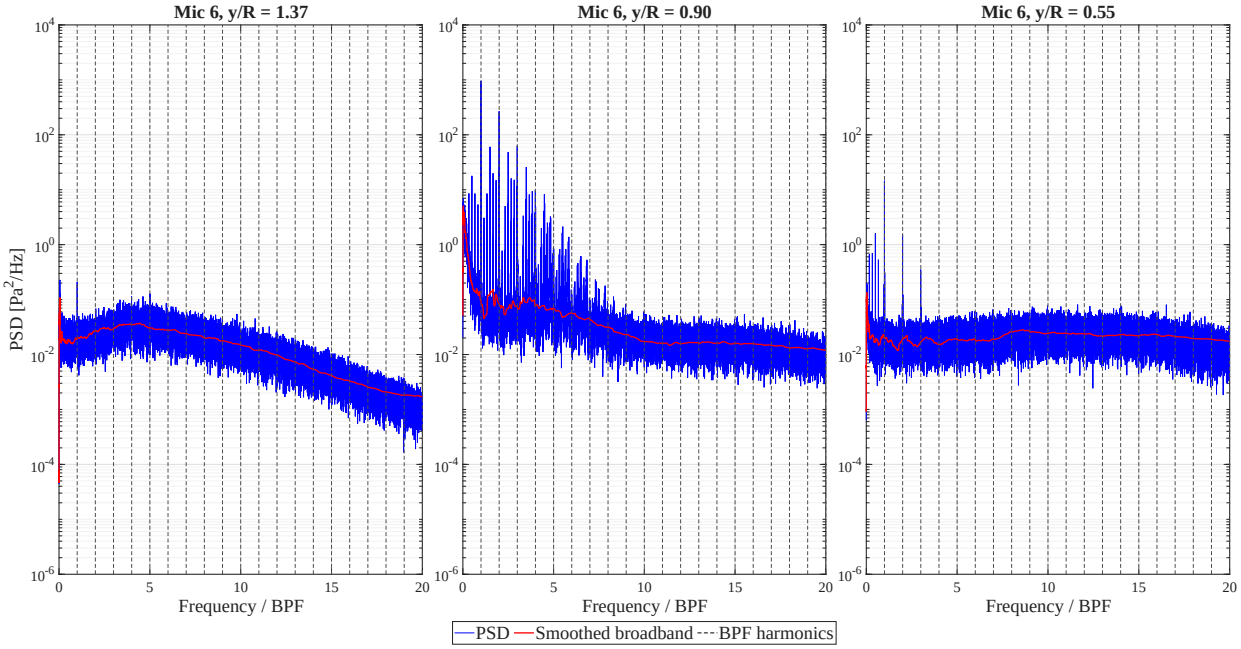

Figure 4.13: PSD of the propeller on case in the suction side at $\alpha = 12^{\circ}$.

A consistent trend across the PSD plots at varying AOAs is the observation of tonal spikes, both outside and within the propeller slipstream. Since the blade is passing through the tip vortex region, a BPF-normalised frequency domain would result in tonal spikes, as the microphones capture the fluctuations caused by the blade tip. The existence of tonal spikes outside the tip vortex region suggests that the noise generation here is being influenced by unsteady loading from both tip vortex impingement and broader turbulent structures in the slipstream and surrounding flow [41].

4.1.4.4. Verification of Flow Regimes in Downgoing Blade Side

As mentioned previously in subsubsection 4.1.4.1, on the downgoing blade side, the airfoil seems to transition early on in the leading edge and the flow is most likely turbulent. In order to verify this, the PSD of the three AOA cases can be used to verify the state of the flow regime. This has been plotted in Figure 4.14.

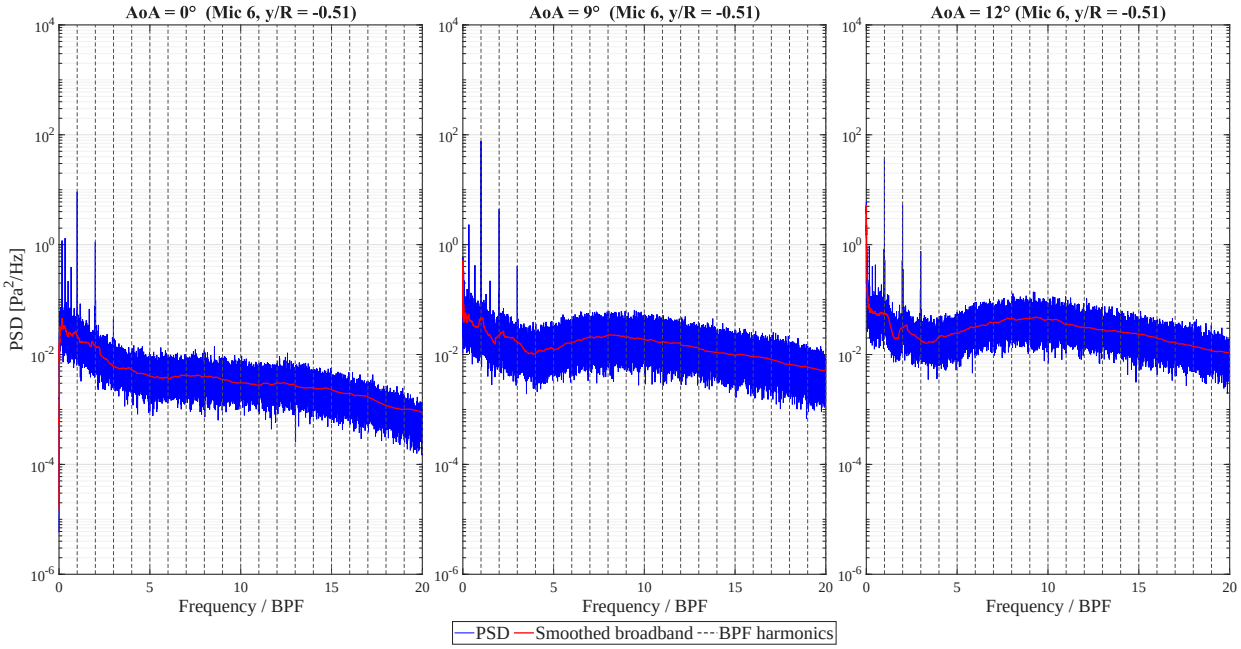

Figure 4.14: PSD of the propeller on cases in the downgoing blade section of the suction side of the airfoil at $x/c = 0.165$.

The $\alpha = 0°$ case exhibits lower broadband energy as compared to the higher angles of attack which is expected as the pressure gradient is more favourable. However, it can be observed from all three cases that the PSD levels are akin to that of a turbulent flow thereby validating the earlier hypothesis that on the downgoing blade side, due to a combination of the increased Reynolds number but also reduced local AOA, the flow is more resemblant to a turbulent flow and thereby resists flow separation more than the upgoing blade side as was observed in Figure 4.9.

4.1.4.5. Effect of Varying Advance Ratios

Figure 4.15 shows the variation of the OFvs across the airfoil when the advance ratio is varied at fixed angle of attack. At $J = 1.8$, the resulting thrust coefficient is significantly lower than for the J 0.8 case (see Figure 3.7). Consequently, the slipstream-induced loading on the airfoil is much weaker at $J = 1.8$. The lower propeller rotational speed reduces both the amplitude of the velocity perturbations and the blade-passage (and hence reduced) frequency of the forcing, so that the boundary layer experiences a smaller-amplitude, more quasi-steady response compared to the $J = 0.8$ case.

Outside the propeller slipstream, it can be observed (Region 2A) that the LSB occurs at the same chordwise location for both the advance ratio cases. Within the propeller slipstream, however, it can be observed that the $J = 1.8$ case showcases the presence of a LSB within the propeller slipstream (Region 2B) which cannot be observed in the lower J case. The difference in forcing provides a plausible explanation for the observed laminar separation bubble behaviour. The weaker and lower-frequency forcing in the $J = 1.8$ case is insufficient to suppress laminar separation so a LSB exists within the slipstream. In contrast, at $J = 0.8$, the strongly loaded slipstream introduces high-amplitude and high-frequency disturbances that promote early transition and strongly energise the boundary layer, removing the time-averaged signature of a laminar separation bubble.

It was, however, observed in Figure 4.9b and Figure 4.9c that there was a LSB within the propeller slipstream at higher AOAs at $J = 0.8$. This suggests that at $\alpha = 0°$, the LSB is either fully suppressed or its separation and reattachment are highly intermittent in time.Given the limited temporal resolution of the present OFV measurements, only the time-averaged behaviour can be assessed, and it can

therefore be concluded that no stable laminar separation bubble is present within the $J = 0.8$ slipstream at $\alpha = 0°$. Intermittent separation and reattachment cannot be ruled out, but would require time-resolved or phase-resolved unsteady measurements to confirm.

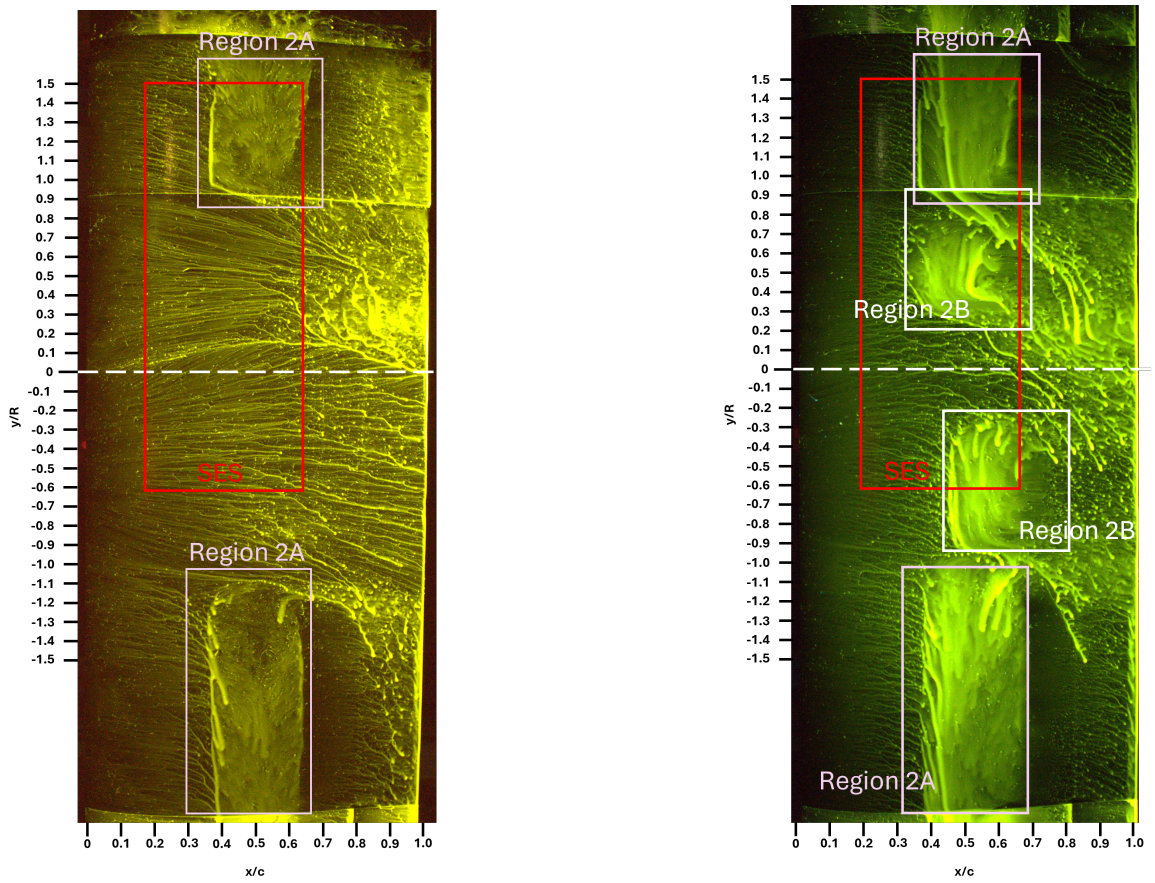

(a) $J = 0.8$ **(b)** $J = 1.8$

Figure 4.15: OFV of the propeller on cases in the suction side for the $J = 0.8$ and $J = 1.8$ case at an AOA of $0°$. Regions 2A and 2B represent the LSB outside and within the propeller slipstream.

Another observation in Figure 4.15b is that the LSB on the upgoing blade side is further upstream as compared to the LSB on the downgoing blade side. This is because on the upgoing blade side, the local angle of attack is increased due to the positive swirl of the propeller causing the LSB to move upstream. At the same time, the downgoing blade side induces a negative swirl causing the local AOA to decrease and the LSB moves further downstream. It can also be noted that the onset of the LSB on the upgoing blade side is slightly further upstream within the slipstream as compared to out of the slipstream further suggesting that the local AOA is the reason why there exists a difference between the locations of the LSB.

At $y/R = 0$, due to the presence of the nacelle, there is no LSB in the region. The flow coming to the airfoil sits in the nacelle wake, which is already thick and potentially turbulent. The nacelle wake acts as a natural trip: the boundary layer on the airfoil is turbulent essentially from the leading edge, so there is no laminar portion that can separate, transition and reattach to form a laminar separation bubble. The nacelle also potentially ”shields” the airfoil from experiencing the stronger propeller-induced flow acceleration so the local pressure gradient in that region is most likely lower than in the regions directly under the slipstream. The combination of wake-induced early transition

and a modified (weaker) pressure distribution in the nacelle wake removes the conditions required for an LSB, which is why it cannot be observed at $y/R = 0$.

In order to verify the inferences drawn above, the PSD distributions for the two advance ratios are compared at the upgoing blade side, nacelle and downgoing blade side positions, as shown in Figure 4.16 and Figure 4.17. It is evident that the $J = 1.8$ case exhibits substantially lower broadband energy levels than the $J = 0.8$ case at all three spanwise locations. The reduced broadband content at $J = 1.8$ indicates a less turbulent, more weakly excited boundary layer, which is therefore more susceptible to laminar separation under the prevailing adverse pressure gradient. This behaviour is consistent with the presence of a laminar separation bubble in the $J = 1.8$ case and its absence in the $J = 0.8$ case observed in the OFVs at Figure 4.15, where the higher turbulence levels inferred from the PSD are expected to stabilise the boundary layer against separation.

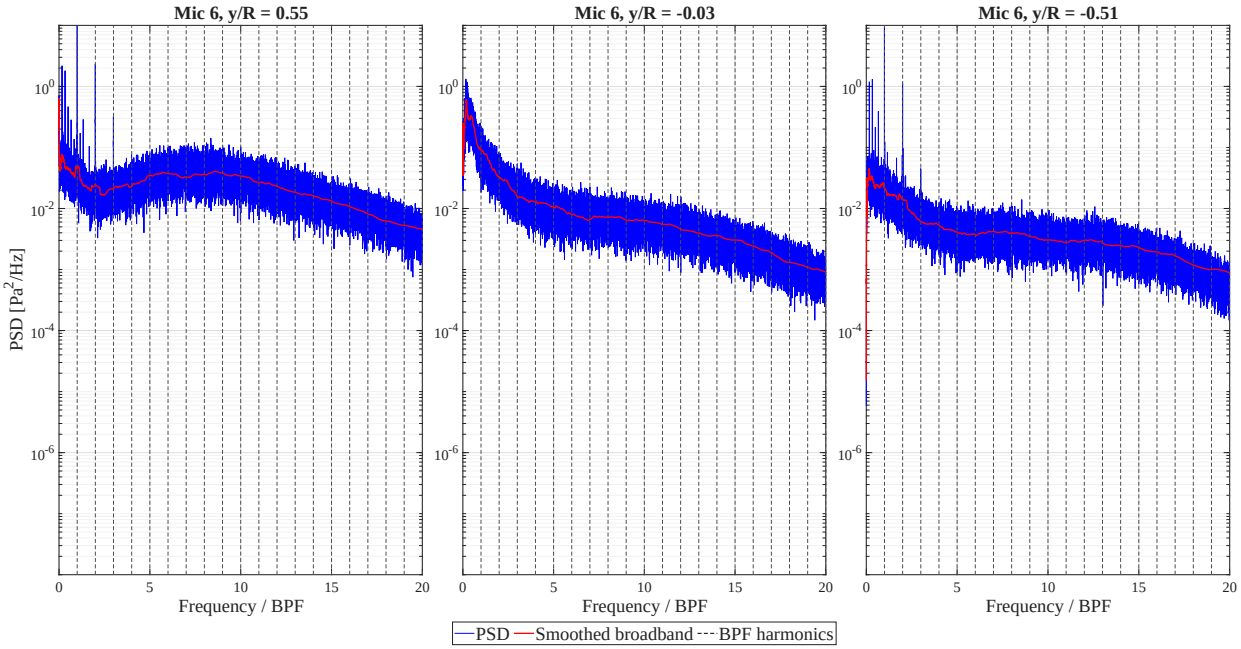

Figure 4.16: PSD of the propeller-on case on the suction side at $\alpha = 0°$ and $J = 0.8$. The microphones at $y/R = 0.55$, -0.03 and -0.51 correspond to the upgoing blade side, nacelle and downgoing blade side regions, respectively.

Furthermore, Figure 4.17 shows that, for $J = 1.8$, the nacelle region exhibits markedly higher broadband levels than the propeller slipstream locations. This confirms that the flow in the wake of the nacelle is more turbulent than in the slipstream, which is consistent with the absence of an LSB in the nacelle region observed in the oil-flow visualisation in Figure 4.15b. The downgoing blade side exhibits lower broadband energy than the upgoing blade side, indicating a weaker level of turbulent forcing and a less aggressive effective pressure gradient. This asymmetry is plausibly linked to the swirl-induced modification of the local inflow angle, which increases the effective AOA on the upgoing side and reduces it on the downgoing side, thereby enhancing the tendency for the LSB to move upstream on the upgoing side relative to the downgoing side.

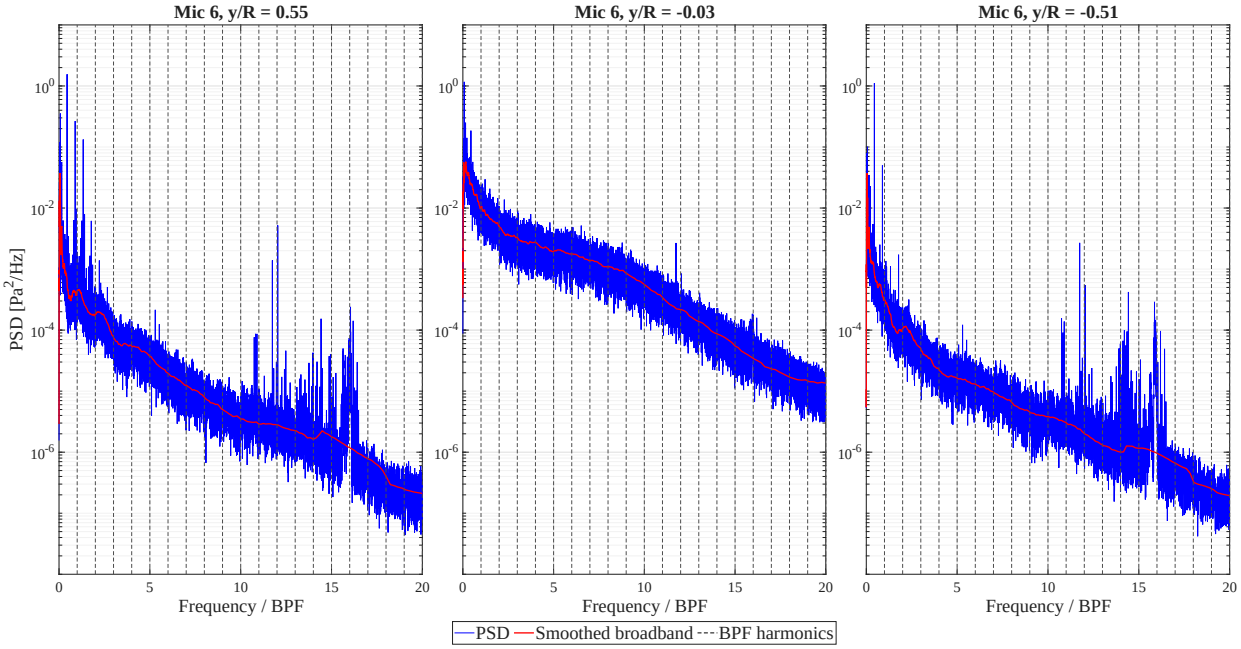

Figure 4.17: PSD of the propeller-on case on the suction side at $\alpha = 0^\circ$ and $J = 1.8$.

4.2. Phase 2 - sPIV Campaign

The first experimental campaign provided a global overview of how the slipstream modifies the boundary layer flow regime on a lifting surface, including the formation of laminar separation bubbles and the associated transition footprint. These results provide a spatially integrated view of where the slipstream has a significant influence, but they do not resolve the underlying three-dimensional flow structures responsible for the observed behaviour. The following sections therefore focus on a second, flat-plate experiment in which sPIV is employed to characterise the coherent vortical structures within the slipstream and their interaction with the near-wall region. While geometric realism is sacrificed as the flat plate is not a lifting surface, this configuration allowed for the study of the instantaneous shear layer, vortex dynamics and slipstream–boundary-layer interaction mechanisms identified in the first campaign, in greater detail.

In this section, the results from the second experimental campaign described in section 3.2 will be discussed, where sPIV was conducted over a flat plate with an elliptical leading edge to understand the effects of the propeller slipstream on the boundary layer. sPIV images were acquired for the following cases:

1. Clean airfoil case with the propeller switched off, representing an unobstructed flow condition.
2. Time-averaged measurements with the propeller operating.
3. Phase-locked measurements with the propeller operating, synchronised with the encoder using a stroboscope.

4.2.1. Time-Averaged Velocity Fields

The time-averaged velocity fields can be used to understand the interactions between the propeller slipstream and a downstream surface. Figure 4.18 showcases the variation in the velocity profiles in the U direction across the three orthogonal planes within the measurement domain.

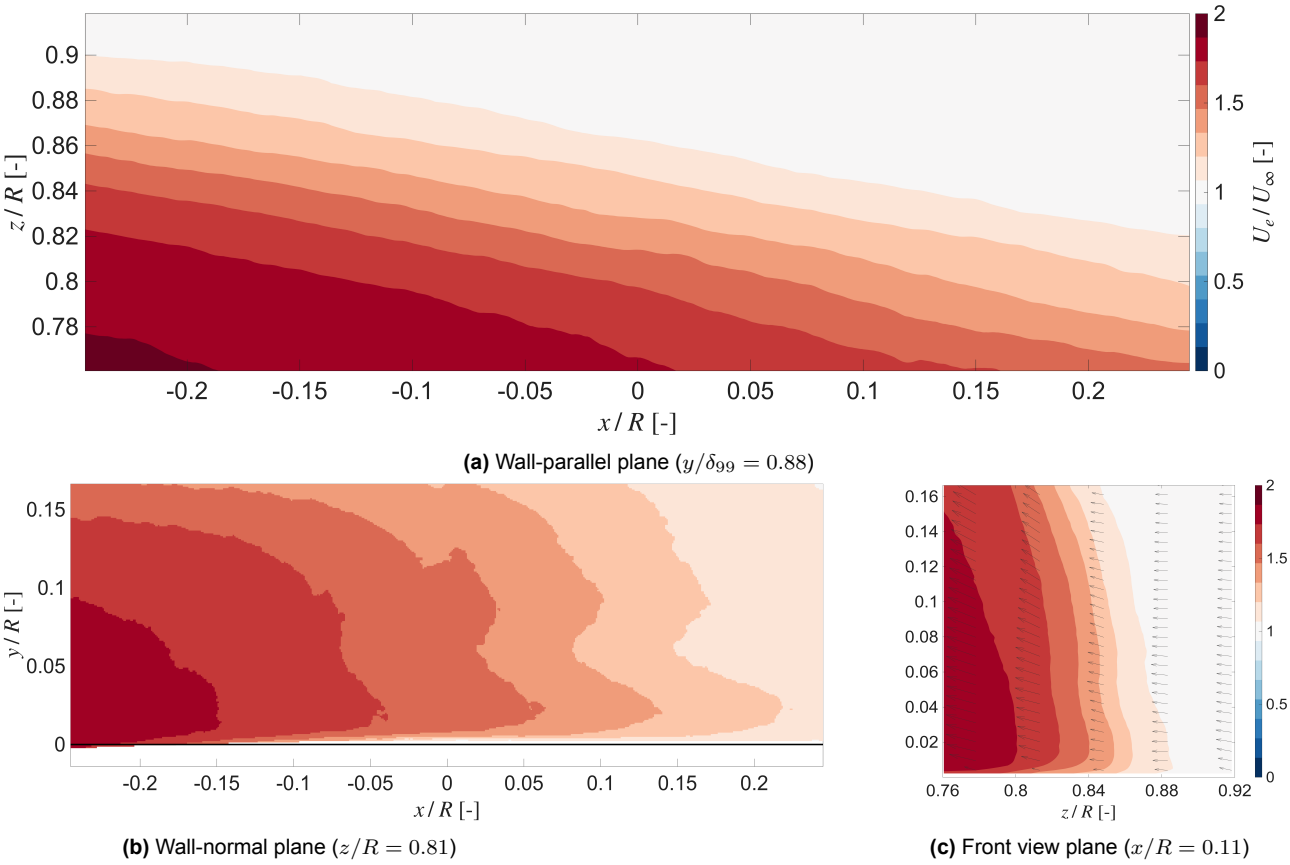

(a) Wall-parallel plane ($y/\delta_{99} = 0.88$)

(b) Wall-normal plane ($z/R = 0.81$)

(c) Front view plane ($x/R = 0.11$)

Figure 4.18: Time-averaged u velocity fields normalised by freestream velocity. Light grey arrows indicate direction of flow.

The propeller adds momentum to the flow within its slipstream and this can be observed in Figure 4.18a, a wall-parallel slice taken at 3 mm off the flat plate surface. In the deepest point of the slipstream, closer to the propeller, the slipstream reaches almost 2 times the velocity of the freestream air. The inner part of the slipstream is a region of increased dynamic pressure accompanied with an increase in local Reynolds number. Another interesting observation from Figure 4.18a is that the slipstream has a tendency to shear inwards from the blade tip to the nacelle hub with the flow accelerating inward along the spanwise direction. This can further be confirmed by Figure 4.18b. The relative orientation of the slice to the spanwise shearing effect results in the axial velocity gradient observed. Along the chordwise direction, the flow velocity reduces as the slipstream shears further into the domain.

Figure 4.18c presents a front view of the taken close to the start of the measurement domain. Apart from the observation of the slipstream shearing inwards in the spanwise direction, it can also be noted that the propeller swirl, marked by the vector arrows on the plot, seem to be accelerating the flow field. There also seems to be crosswise increase in velocity which can most likely be attributed to the helical nature of the vortex structures in the slipstream system. This will be discussed in further in later chapters using the phase-locked measurements.

4.2.2. Variation of Boundary Layer Thickness (δ_{99})

The propeller slipstream also induces a local variation in the boundary layer thickness in the spanwise direction which has been discussed in this section using Figure 4.19 which represents the increase in boundary layer thickness as compared to a propeller off case.

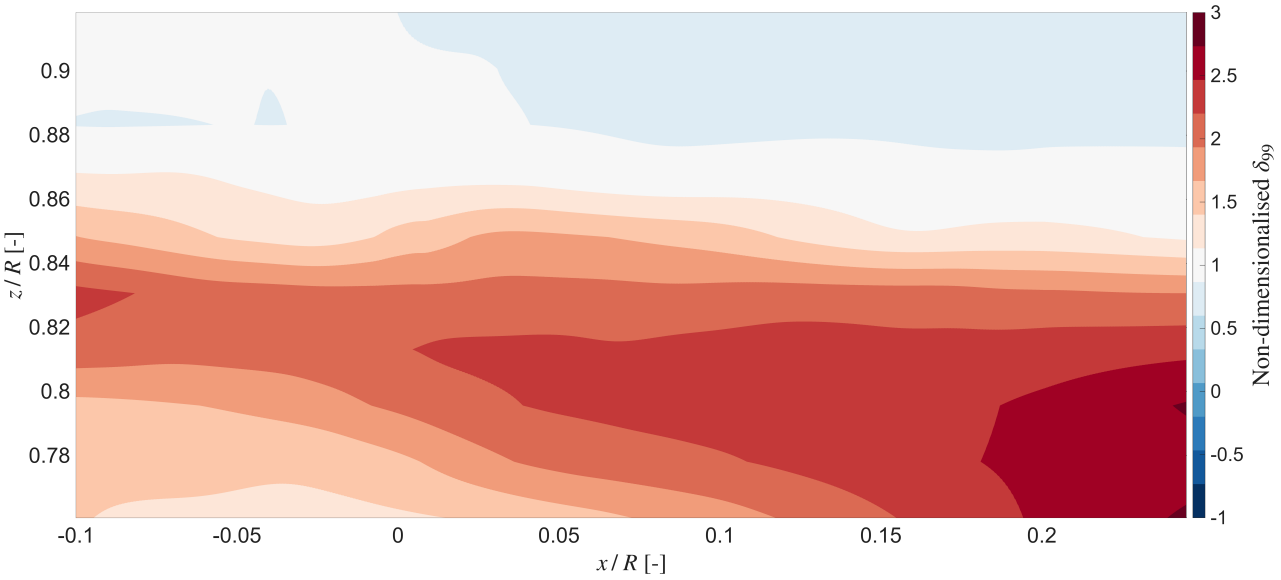

Figure 4.19: Relative change in boundary layer thickness between the propeller on case and the clean case.

A relative change in the time-averaged δ_{99} between the propeller on and the propeller off case has been used as a metric to quantify the change the fluctuation in the boundary layer as a result of the slipstream. It can be observed that the boundary layer seems to thicken more on the inboard side of the slipstream edge, with the thickest section at the farthest inboard point of the measurement domain. As expected, it increases in the chordwise direction as the boundary layer grows. For z/R values greater than around 0.86, it seems that the vortex structures are fairly weak and do not result in any thickening of the boundary layer. The slipstream persistently amplifies boundary-layer growth downstream rather than acting as a purely local disturbance.

While the blue regions indicate a boundary layer thinning, it is not possible to conclusively suggest that as near the blade tip, the boundary layer was extremely thin to be resolved accurately. While it may be possible to conclusively suggest that the slipstream does cause the boundary layer to thicken in a time-averaged sense, the same cannot be said for the region outside the dominant vortex structures.

4.2.3. Phase-Locked Vorticity Fields

The vorticity plots for a laminar boundary layer versus a turbulent boundary layer have been plotted in Figure 4.20. The turbulent boundary layer was achieved by transitioning the boundary layer at the leading edge using a trip strip while the laminar boundary layer represents the untripped flow. As the tripped and untripped flows exhibit different boundary-layer thicknesses, the wall-parallel positions were chosen to represent the same non-dimensionalised location within each boundary layer, ensuring a fair comparison.

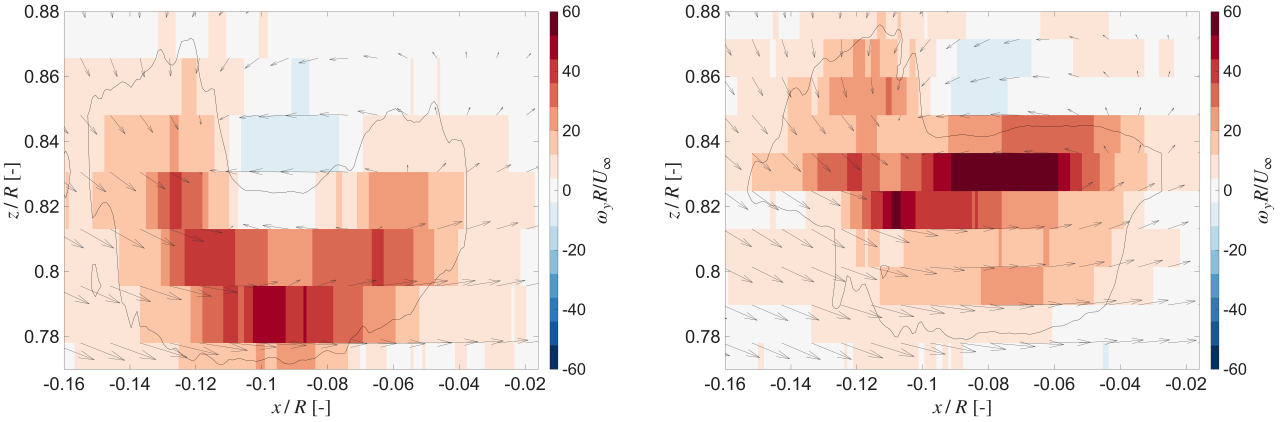

(a) Untripped flow

(b) Tripped flow

Figure 4.20: Non-dimensionalised vorticity ($\frac{\omega_y R}{U_\infty}$) at $y/\delta_{99} = 0.59$. Black line indicates approximate shape of the primary vortex structure. Light grey arrows represent the U velocity vectors.

It can clearly be observed that the vorticity is much stronger in the turbulent boundary layer from Figure 4.20b. In addition to the increase in magnitude, several qualitative differences emerge between the two cases. In the untripped, laminar boundary layer, the region of strong positive vorticity is relatively compact and confined to a narrow band with only a few grid cells reaching a vorticity of over 40. In contrast, the tripped turbulent boundary layer exhibits a much larger, contiguous core of high positive vorticity that extends over a broader streamwise range and slightly higher z/R. The absolute height of the wall-parallel slice is larger in the tripped flow is larger due to the thicker boundary layer. However, the vorticity is still higher at this greater physical distance from the wall, suggesting that the near-wall shear and associated vorticity production are significantly enhanced by turbulence. The turbulent boundary layer thus supports a thicker region of elevated vorticity, rather than a thin shear layer confined very close to the wall as in the laminar case. Turbulent boundary layers possess steeper mean velocity gradients and enhanced mixing, which in turn generate higher vorticity levels and more coherent near-wall vortex structures.

4.2.4. Analysis of Phase-Locked TKE Fields

The non-dimensionalised Turbulent Kinetic Energy (TKE) has been plotted for the same boundary layer length scale for both the untripped and tripped flows in Figure 4.21 and Figure 4.22.

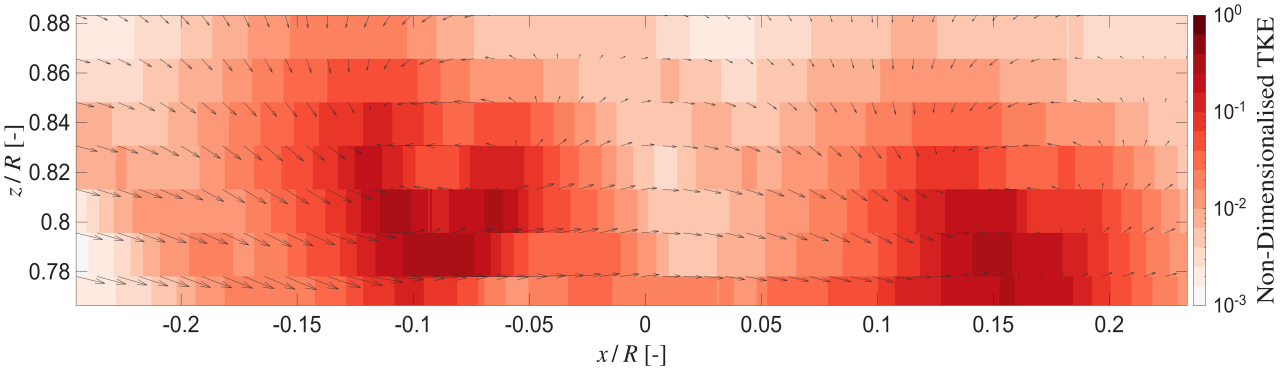

Figure 4.21: TKE of the untripped flow at $y/\delta_{99} = 0.59$ and $\phi = 140°$. Light grey arrows represent the U velocity vectors.

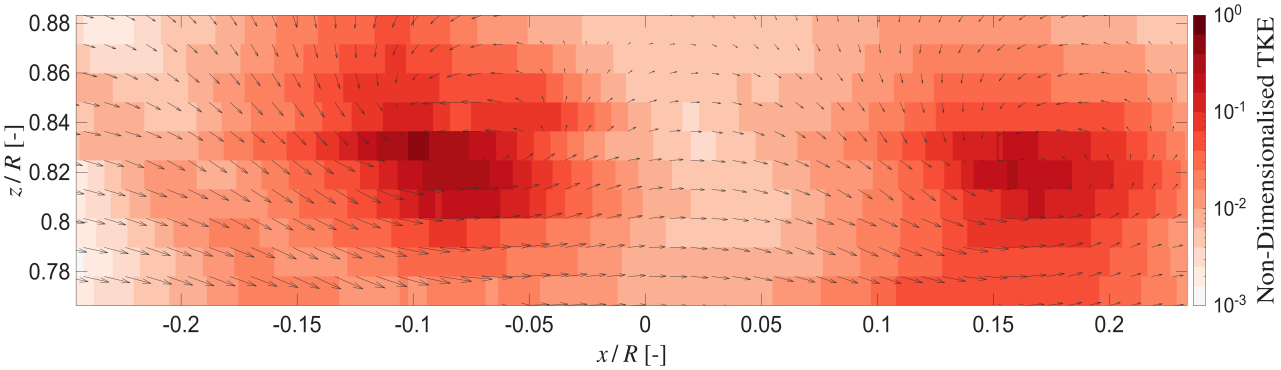

Figure 4.22: TKE of the tripped flow at $y/\delta_{99} = 0.59$ and $\phi = 140°$. Light grey arrows represent the U velocity vectors.

It can be observed that in both cases, the values for TKE are comparable for the same y/δ_{99}. Inside the propeller slipstream, the untripped boundary layer does not remain laminar but undergoes bypass transition due to the intense unsteady forcing from the helical wake, blade-passage disturbances, and the strong local shear. As a result, by the time the flow reaches the PIV measurement plane, both the tripped and untripped cases have developed into fully turbulent boundary layers, and the near-wall dynamics are dominated more by the slipstream forcing than by the presence or absence of the trip strip. When TKE is being compared at the same normalised wall-parallel location, the two cases therefore show similar turbulence levels, because y/δ_{99} collapses the inner and outer-layer structure and both boundary layers have comparable wall-shear scaling and similar levels of propeller-induced unsteadiness. Consequently, the trip strip primarily affects transition upstream and the overall boundary-layer thickness, but has limited influence on the local turbulence intensity within the region directly forced by the slipstream.

Figure 4.23 shows the variation in TKE in a phase-locked sense close to the outboard side of the slipstream ($z/R = 0.85$). Between approximately -0.2 x/c and -0.1 x/c, the blade wake can be visible. Each blade of the propeller sheds a thin wake sheet downstream of its trailing edge, carrying the blade's viscous losses and any small trailing-edge separation. Between -0.05 x/c to 0 x/c, the vortex core is clearly visible, characterised by a large increase in TKE as compared to outside the core.

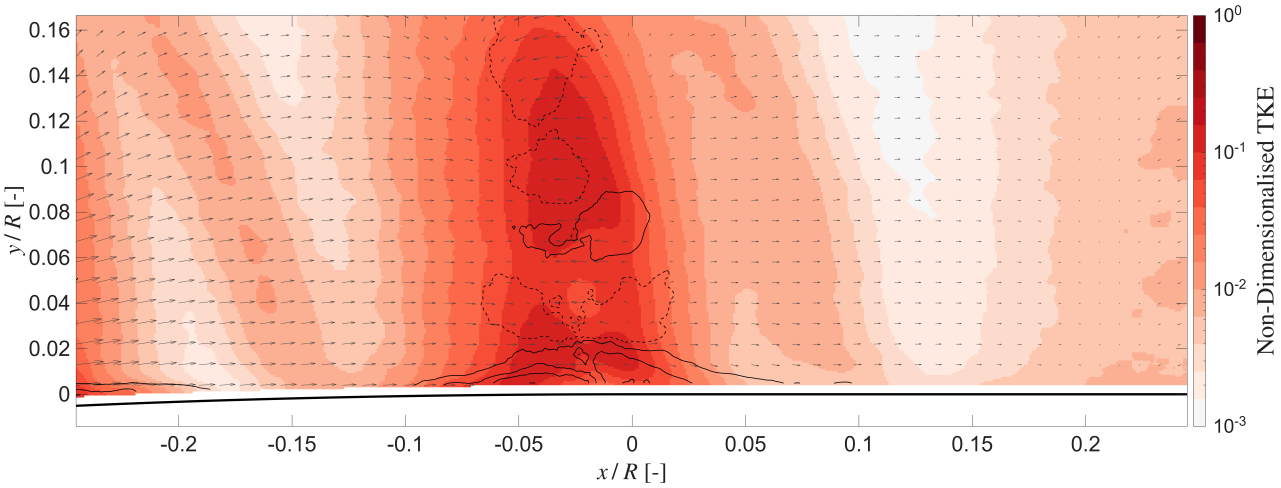

Figure 4.23: Phase-locked TKE at $\phi = 60°$ and $z/R = 0.85$.

A key outcome of this phase-locked view is the clear laminar-turbulent intermittency of the boundary layer under the effect of the slipstream. This was a theory first put forth by Miley and Holmes, where they used flight and wind tunnel data to determine the existence of patches of laminar flow between travelling regions of turbulence [14]. In Figure 4.23, between the wake sheets and away from the vortex core, large patches of very low TKE appear (light colours), indicating phases where the near-wall flow is close to laminar or only weakly turbulent despite the time-averaged field being fully turbulent. Physically, successive wake-impingement events trigger short, intense bursts of turbulence and elevated shear; in the intervals between passages, the local acceleration inside the slipstream and the absence of strong external disturbances allow partial re-laminarisation or at least a strong reduction of turbulent activity. The time-average smears these alternating states into a uniformly high-TKE picture, whereas the phase-locked map shows that the high levels are produced intermittently in space and phase.

4.2.5. Analysis of 3D Vortex Structures

The coherent vortical structures have been visualised using the normalised Q-criterion ($q = qR^2/U_\infty$) isolating rotationally dominant regions of the fluid. Figure 4.24 shows iso-surfaces of q at a phase angle of $140°$, together with a wall-parallel slice taken at a y/δ_{99} of 0.89. Within the measurement domain, there exists a tip vortex system between approximately 0.78 - 0.85 z/R. The system consists of two vortex cores which have been captured over the full streamwise extent of the domain, together with a weaker structure at the upstream boundary that is consistent with the onset of the blade wake. The vortex system also has two parts, a primary slipstream vortex and a secondary vortex structure that seems to be emanating from the wall.

The primary vortex structure exhibits a three-dimensional character largely focused in the wall normal y-direction which can be attributed to the incoming tip vortex from the propeller. Away from the wall, the corresponding q-isosurfaces exhibit a helical structure with a slight positive inclination the streamwise (x-direction) and a slight negative inclination in the spanwise (z-direction) direction. On the outboard side, there appears to be a split in the vortex structure emerging from the slipstream. The axial vorticity embedded in the tip vortex diffuses into, and interacts with, the streamwise vorticity present in the boundary layer; depending on the local sign of vorticity, this interaction can either erode or amplify portions of the primary vortex. The result is a progressive deformation of the vortex tube, followed by its division into multiple thinner filaments. Some filaments remain surface-attached and are stretched downstream, while others detach and are convected upwards, giving the impression of a broken or hollowed-out vortex core [21].

The secondary vortex structure seems to be emerging from the boundary layer of the flat plate and wraps around the primary vortex as it flows downstream (Figure 4.26). Close to the wall, the secondary vortex exhibits streamwise and spanwise vorticity components consistent with an origin in the boundary layer. The secondary vortex structure on the wall appears to be a result of the flat plate's boundary layer vorticity mixing with the vortex system from the propeller. As this structure convects upward and inward, the structure becomes more three-dimensional indicating its convergence with the primary vortex structure. This can be observed from the vorticity vectors on the inboard side of Figure 4.24.

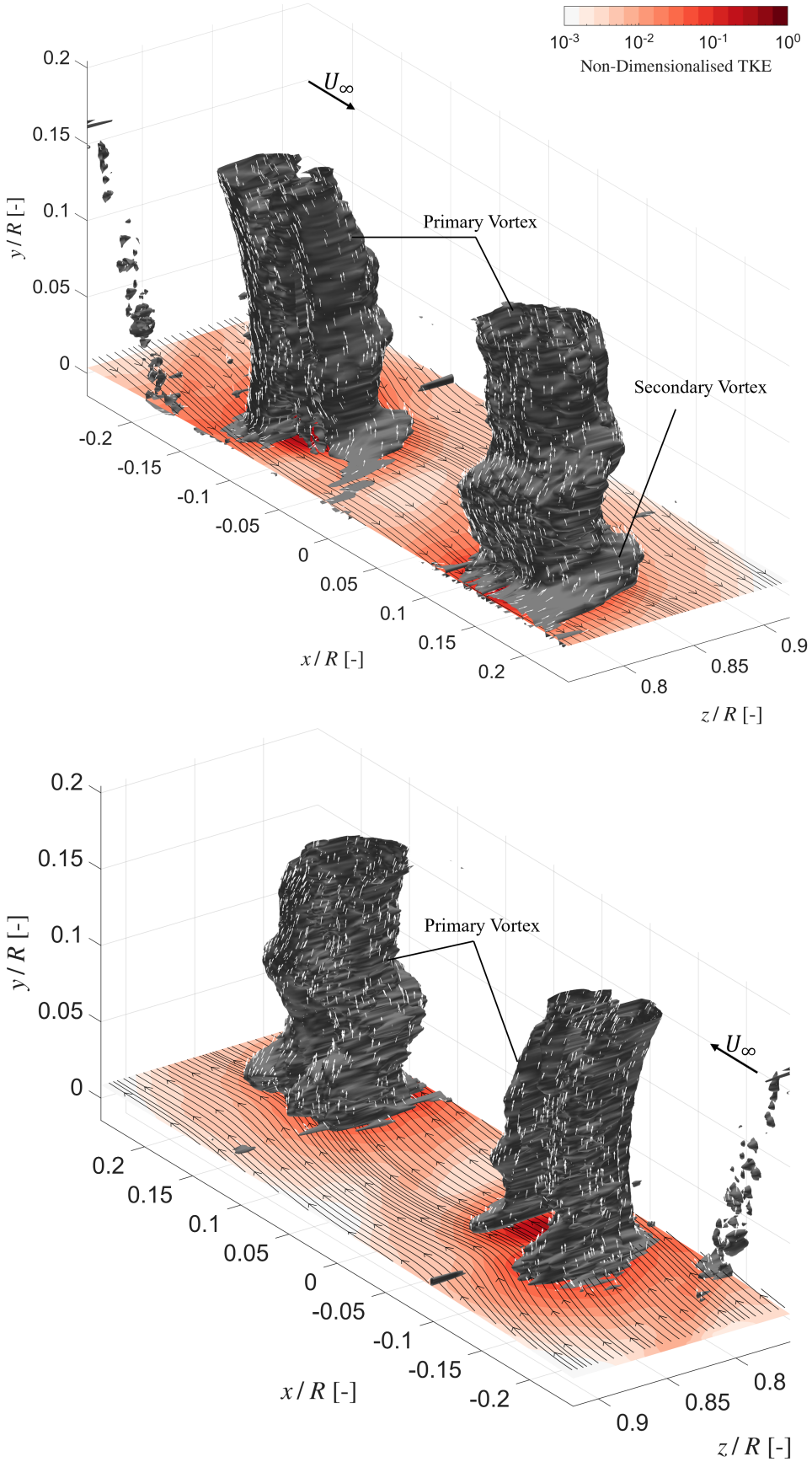

Figure 4.24: Isosurfaces of vortex core regions at a phase angle of $140°$. The slice is taken at a y/δ_{99} of 0.89. White vectors indicate local vorticity vectors. Contour plot represents the non-dimensionalised TKE. First plot is inboard side; upstream view. Second plot is outboard side; downstream view. Black arrows indicate direction of streamlines.

Another observation that can be made from Figure 4.24 is that as the vortex core passes, the TKE increases suggesting that the slipstream induces some level of turbulence locally. This verifies what was suggested earlier in subsection 4.2.4 that the vortex core causes intermittent patches of turbulence to exist in what is mostly a laminar flow.

Additionally, when the vortex system was plotted against the contour of the non-dimensionalised flow velocity (Figure 4.25), it could be observed that the inboard side of the slipstream experienced a higher flow velocity as compared to the outboard side. This local shear along the vortex system could have potentially amplified the boundary layer vorticity. The resulting spanwise gradients, in combination with the amplified boundary layer vorticity, facilitate the development of the secondary vortex structure which couples with the primary vortex to feedback into the overall 3-D interaction.

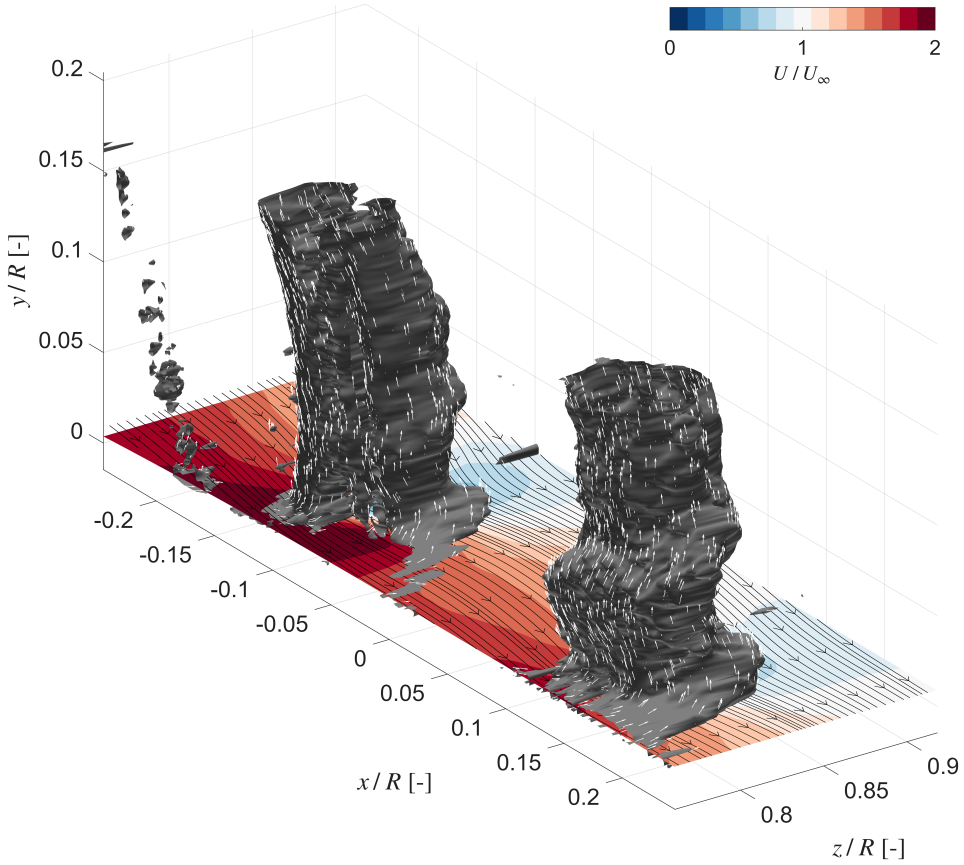

Figure 4.25: Inboard side of the vortex core region at a phase angle of $140°$. The slice is taken at a y/δ_{99} of 0.89. Contour plot represents the non-dimensionalised U velocity.

Figure 4.26 shows how the vortex system modulates the flow in the wall-normal direction. Across all phases, the passage of the primary vortex is accompanied by localised patches of positive and negative V/U_∞ with magnitudes of order $0.1U_\infty$, indicating a strong, highly three-dimensional exchange of momentum between the boundary layer and the outer flow. On the inboard side, bands of V/U_∞ form adjacent to the vortex core and elongate in the streamwise direction as the phase advances from $\phi = 60°$ to $140°$, consistent with a lift-up of near-wall fluid into the slipstream interior as the primary vortex convects downstream. On the outboard side, regions of opposite-signed V/U_∞ appear on either side of the vortex cores, indicating complementary downward motions that push higher-momentum fluid towards the wall and close the induced circulation of the vortex pair.

The phase evolution in Figure 4.26 also illustrates the progressive emergence of the secondary vortex. At $\phi = 60°$ the secondary structure is only weakly expressed in the V/U_∞ field and remains confined close to the wall. By $\phi = 100°$ and $140°$, distinct lobes of wall-normal velocity are observed around the secondary core, particularly on the outboard side, where they wrap around the primary vortex and extend further downstream. The regions of largest $|V|$ velocity are located with the high-speed inboard belt of the slipstream identified in Figure 4.25, suggesting that the strongest lift-up and subsequent roll-up of boundary-layer vorticity occur where the local slipstream acceleration is greatest. This behaviour supports the earlier inference that the secondary vortex structure originates from the boundary-layer vorticity that is lifted, stretched and entrained by the primary vortex, rather than being shed directly from the propeller, and it links the three-dimensional vortex dynamics to the laminar–turbulent intermittency discussed earlier.

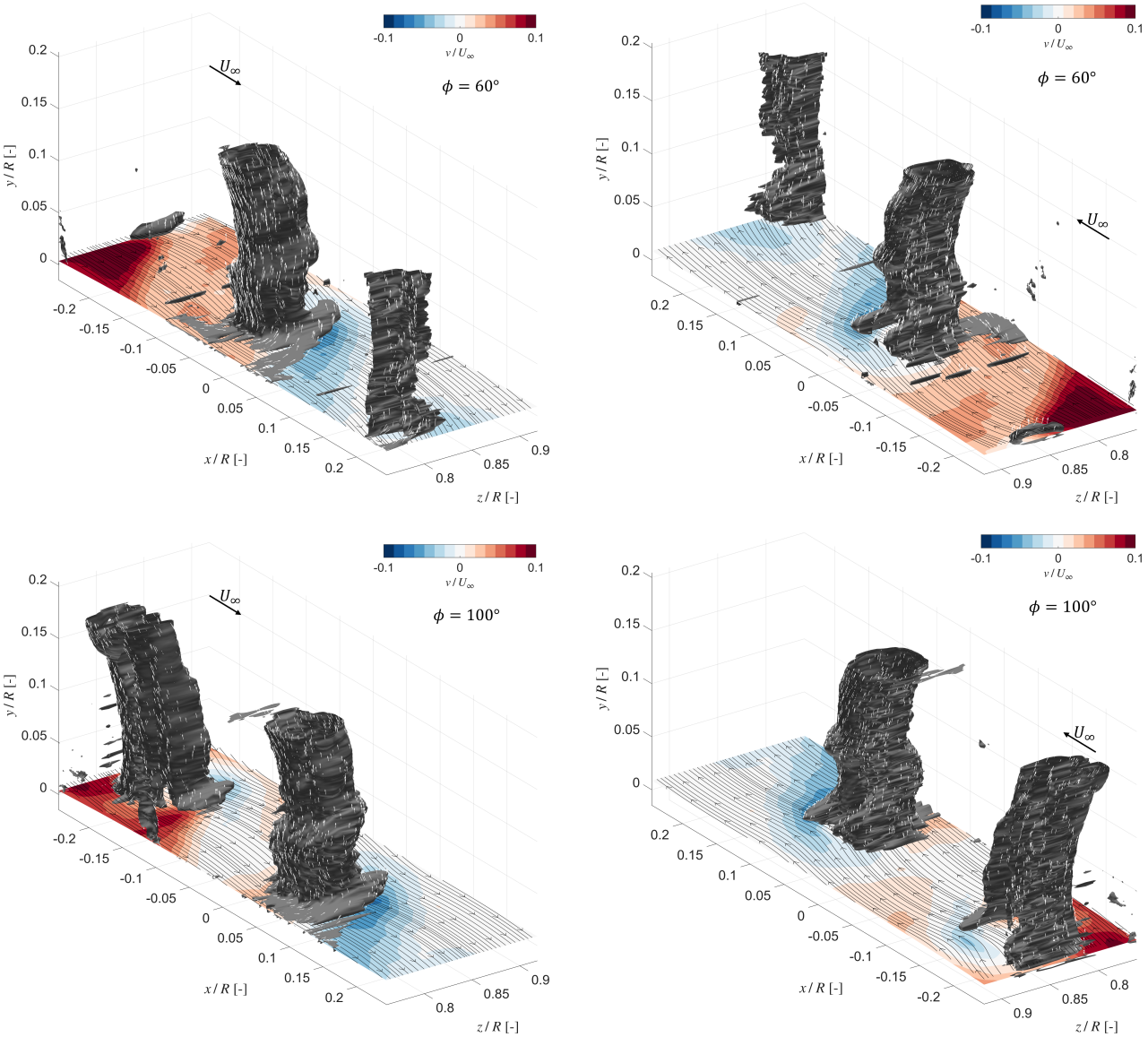

Figure 4.26: Isosurfaces of vortex core regions at phases $\phi = 60°, 100°$ and $140°$. Contour slices represent the V velocity normalised to the freestream velocity. Left column: inboard side, upstream view; Right column: outboard side, downstream view.

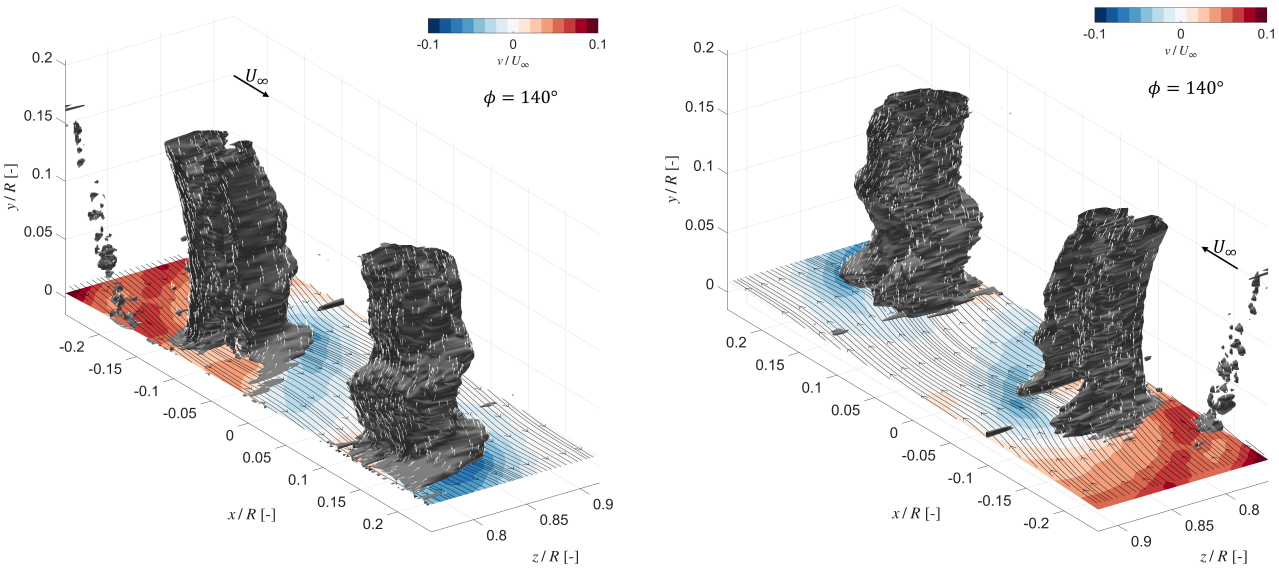

Figure 4.26: Isosurfaces of vortex core regions at phase 140° (continued).

5

Conclusion and Recommendations

This chapter summarises the notable findings, limitations and future recommendations for the two experiments.

The thesis investigated the effects of a propeller slipstream on a wing's boundary layer, drawing conclusions from two experimental campaigns. In the first campaign, a novel flexible PCB-based measurement device embedded with microphones and pressure sensors was used to capture variations in SPL, complemented by oil-flow visualisations to qualitatively characterise the flow field. The second campaign employed sPIV to capture time-averaged and phase-locked states of the boundary layer. The research was motivated by the need to better understand slipstream–boundary-layer interactions, particularly variations in flow regime and the role of vortical structures within the slipstream. As many previous studies have focused solely on time-averaged measurements, which do not fully resolve the slipstream dynamics, this work addresses that limitation. Phase 1 used acoustic and oil-flow measurements to identify where the slipstream modified the downstream boundary-layer regime, whereas Phase 2 employed velocity and vorticity measurements to resolve the three-dimensional vortex system and near-wall turbulence responsible for those signatures. Together, the two campaigns provide complementary diagnostic and mechanistic perspectives on the same slipstream–boundary-layer interaction. The study could be extended to examine the effects of angle of attack and advance ratio, and to include twin-propeller configurations to evaluate and optimise DEP systems.

5.1. Findings

Across both experimental phases, there are notable conclusions that emerge. First, the propeller slipstream strongly energises the downstream boundary layer and promotes early transition, but this effect is highly non-uniform in both span and phase. Second, the slipstream can either generate or suppress laminar separation bubbles depending on the amplitude of the slipstream and effective AOA. Third, the interaction is inherently three-dimensional and intermittent, governed by a coupled system of tip and secondary vortices that drive near-wall bursts of high shear and turbulence. The phase-specific findings elaborate on these points. The findings from this study have been explained in detail below:

5.1.1. Phase 1 - SES and OFV Measurements

- For the nacelle-only cases, an LSB is present. As AOA increases, the APG strengthens, the LSB moves upstream, and the separation point shifts upstream. These trends are reflected in

the SPL maps: turbulent reattachment at the end of the LSB produces local SPL peaks, while separated regions exhibit lower broadband SPL than attached turbulent flow.

- With the propeller operating, outside the slipstream, the LSB behaves similarly to the nacelle-only cases but moves upstream and shortens with increasing AOA. Within the slipstream, at high AOA, a separation region and LSB can be observed on the upgoing blade side only. The postulation is that due to a combination of Reynolds effects and reduced local AOA, the downgoing blade side experiences turbulent inflow causing the flow to remain attached while also not showing any LSB.
- When the advance ratio was varied from $J = 0.8$ to $J = 1.8$ at an AOA of $0°$, outside the propeller slipstream, the LSB forms at the same chordwise location, indicating that the baseline boundary-layer behaviour is unchanged. However, within the slipstream, a LSB is only observed for the lower amplitude slipstream, produced by the $J = 1.8$ case but for the stronger amplitude slipstream, produced by the $J = 0.8$ case, the stronger loading removes the time-averaged LSB signature.
- PSD analysis across representative spanwise locations shows that broadband levels and spectral shape are strongly AOA-dependent: energy is lowest outside the slipstream at $0°$ AOA, increases at $9°$ AOA, with a pronounced outer-slipstream hump consistent with a leading-edge LSB and turbulent reattachment, then decreases again at $12°$ AOA, despite a longer LSB, indicating less efficient instability amplification, while sharp tonal peaks at the BPF and its harmonics persist at all AOAs both inside and outside the nominal tip-vortex region.

5.1.2. Phase 2 - sPIV Campaign

- The time-averaged velocity fields show that the propeller strongly energises the flow within its slipstream: From a wall-parallel perspective ($y/\delta_{99} = 0.89$), the axial velocity in the core reaches almost twice the freestream value, implying locally enhanced dynamic pressure and Reynolds number. The slipstream undergoes inboard shearing with spanwise acceleration towards the nacelle and chordwise decay, while the front-view plane confirms that propeller swirl drives a crosswise velocity increase associated with the helical vortex system. This was also the same phenomena observed in the OFVs in Phase 1, where the streamlines in the upgoing blade section were converging towards the hub.
- A relative increase in time-averaged δ_{99} between the prop-on and prop-off cases shows that the boundary layer thickens preferentially on the inboard side of the slipstream edge, with the largest thickening at the most inboard extent of the measurement domain. Downstream, the boundary layer grows in the chordwise direction as expected, while for z/R 0.86, the vortex structures appear too weak to induce additional thickening. This inboard thickening provides a time-averaged counterpart to the LSB behaviour observed in Phase 1, where separation and reattachment were more pronounced on the upgoing blade side within the slipstream.
- When compared at the same non-dimensional wall-parallel position, the TKE levels for the tripped and untripped flows are very similar, suggesting that, near-wall turbulence is governed primarily by the slipstream forcing rather than by the underlying boundary-layer state. This supports the interpretation from the SES measurements that tonal blade-passage peaks and broadband energy levels within the slipstream are primarily controlled by the imposed unsteady forcing from the propeller, rather than by whether the incoming boundary layer is nominally laminar or turbulent.
- Phase-locked TKE fields reveal laminar–turbulent intermittency within the slipstream, with wake-impingement events producing short bursts of high shear and TKE separated by phases

of weakly turbulent or nearly laminar near-wall flow that are not visible in the time-averaged field.

- The 3D Q-criterion visualisations reveal a tip-vortex system with two cores and a portion of the blade wake: a primary slipstream vortex with strongly 3D, wall-normal structure that splits inboard into thinner filaments, and a secondary vortex originating from the wall. Non-dimensional velocity contours show higher inboard slipstream velocities and enhanced shear, consistent with secondary-vortex formation by spanwise velocity gradients and amplified boundary-layer vorticity. Together, the coupled primary–secondary system creates the 3D interaction between the propeller wake and the flat-plate boundary layer.

5.2. Limitations

Apart from the findings listed above, there are some limitations in the work of this thesis that need to be addressed:

- A significant limitation from the first experiment was the lack of spatial resolution, as the data from the second and third rows of microphones could not be used, resulting in not being able to fully quantify the acoustic measurements from the downgoing blade side region. Furthermore, data near the leading edge could not be captured as the PCB required a flexible design in that region.
- Although the sampling time for the DAQ from SES was set at 30 seconds, the actual recorded time was often below that time and inconsistencies were observed across multiple test cases.
- The flat plate could not produce a pressure gradient, so it was not possible to observe LSBs in the unsteady sense to draw comparisons between the two experiments.
- Variations in AOA and J were not studied during the second experiment. Moreover, in the first experiment, the propeller inflow angle was not varied with the airfoil, so it is not directly comparable to real-life conditions.

5.3. Future Recommendations

The future recommendations of this study include:

- Redesign the SES without integrated pressure sensors to allow a denser microphone layout and hence higher spatial resolution of the acoustic field. In addition, varying the propeller AOA, rather than only the airfoil AOA, would provide operating conditions that are more representative of real applications.
- Replace the flat-plate model in the sPIV campaign with a lifting surface to achieve a closer correspondence with practical configurations. This would enable variation of both angle of attack and advance ratio J, thereby broadening the scope of the study and also comparing it to real-life conditions.

References

[1] Roy D Hager. *Advanced Turboprop Project*. Vol. 495. Scientific, Technical Information Division, National Aeronautics, and Space Administration, 1988.

[2] Manuel A Rendón et al. “Aircraft hybrid-electric propulsion: Development trends, challenges and opportunities”. In: *Journal of Control, Automation and Electrical Systems* 32.5 (2021), pp. 1244–1268.

[3] John D Anderson. “Ludwig Prandtl’s boundary layer”. In: *Physics today* 58.12 (2005), pp. 42–48.

[4] John Anderson. *Fundamentals of Aerodynamics*. McGraw hill, 2011.

[5] Georgios Rigas, D. Sipp, and T. Colonius. “Nonlinear input/output analysis: application to boundary layer transition”. In: *Journal of Fluid Mechanics* 911 (2020). DOI: 10.1017/jfm.2020.982.

[6] T. Zaki. “From Streaks to Spots and on to Turbulence: Exploring the Dynamics of Boundary Layer Transition”. In: *Flow, Turbulence and Combustion* 91 (2013), pp. 451–473. DOI: 10.1007/s10494-013-9502-8.

[7] Rıdvan Salih Kuzu, Philipp Mühlmann, and Xiao Xiang Zhu. “Automatic separation of laminar-turbulent flows on aircraft wings and stabilisers via adaptive attention butterfly network”. In: *Experiments in Fluids* 63.10 (2022), pp. 1–26. ISSN: 0723-4864. DOI: 10.1007/s00348-022-03516-4.

[8] Theodoros Michelis. “Boundary layer separation: Diagnostics and control”. PhD thesis. Delft University of Technology, 2017.

[9] Barnes W McCormick. *Aerodynamics, aeronautics, and flight mechanics*. John Wiley & Sons, 1994.

[10] Robert Nederlof. “Improved modeling of propeller-wing interactions with a lifting-line approach”. MA thesis. MSc. Delft University of Technology, 2020.

[11] A. C. Kermode. *Mechanics of Flight*. 11th. Pearson Education, 2006. ISBN: 978-1-4058-2359-3.

[12] T.C.A. Stokkermans. “Aerodynamics of Propellers in Interaction Dominated Flowfields: An Application to Novel Aerospace Vehicles”. Ph.D. thesis. Delft University of Technology, 2020. ISBN: 978-94-6366-332-8. DOI: 10.4233/46178824-bb80-4247-83f1-dc8a9ca7d8e3. URL: https://doi.org/10.4233/46178824-bb80-4247-83f1-dc8a9ca7d8e3.

[13] L.L.M. Veldhuis. “Propeller Wing Aerodynamic Interference”. Ph.D. thesis. Delft University of Technology, 2005. URL: https://resolver.tudelft.nl/uuid:8ffbde9c-b483-40de-90e0-97095202fbe3.

[14] Stan J Miley, Richard M Howard, and Bruce J Holmes. “Wing laminar boundary layer in the presence of a propeller slipstream”. In: *Journal of Aircraft* 25.7 (1988), pp. 606–611.

[15] Fernando Martini Catalano. “On the effects of an installed propeller slipstream on wing aerodynamic characteristics”. In: *Acta Polytechnica* 44.3 (2004).

[16] Hamzeh Aminaei, Mojtaba Dehghan Manshadi, and Ali Reza Mostofizadeh. “Experimental investigation of propeller slipstream effects on the wing aerodynamics and boundary layer treatment at low Reynolds number”. In: *Proceedings of the Institution of Mechanical Engineers, Part G: Journal of Aerospace Engineering* 233.8 (2019), pp. 3033–3041.

[17] L Riccobene et al. “Wind tunnel test of full-scale wing-propeller system of a eVTOL aircraft”. In: *The Aeronautical Journal* 128.1324 (2024), pp. 1204–1218.

[18] RT Johnston and JP Sullivan. “Unsteady wing surface pressures in the wake of a propeller”. In: *Journal of aircraft* 30.5 (1993), pp. 644–651.

[19] Robert Johnston and John Sullivan. “Propeller tip vortex interactions”. In: *28th Aerospace Sciences Meeting*. 1990, p. 437.

[20] DAVID WITKOWSKI, ROBERT JOHNSTON, and JOHN SULLIVAN. “Propeller/wing interaction”. In: *27th Aerospace Sciences Meeting*. 1989, p. 535.

[21] M Felli. “Underlying mechanisms of propeller wake interaction with a wing”. In: *Journal of Fluid Mechanics* 908 (2021), A10.

[22] Tomas Sinnige et al. “Unsteady pylon loading caused by propeller-slipstream impingement for tip-mounted propellers”. In: *Journal of Aircraft* 55.4 (2018), pp. 1605–1618.

[23] Meilin Yu et al. “Freestream turbulence effects on low Reynolds number NACA 0012 airfoil laminar separation bubble and lift generation”. In: *Aerospace Science and Technology* (2024). DOI: 10.1016/j.ast.2024.109145.

[24] Masaki Okawa et al. “Unsteady Propeller Wake Interference on Wing in Tractor Configuration at Low-Reynolds-Number Condition”. In: *Journal of Aircraft* 62.1 (2025), pp. 3–12.

[25] Donald L Loving and Samuel Katzoff. *The Fluorescent-Oil Film Method and Other Techniques for Boundary-Layer Flow Visualization*. Tech. rep. NASA Langley Research Center, 1959.

[26] LLC Knowles Electronics. *Knowles SPW0690LM4H□1 Microphone*. KAS□700□0146. Product brief. Knowles Electronics, LLC. Itasca, IL, USA, 2019. URL: https://media.digikey.com/pdf/Data%20Sheets/Knowles%20Acoustics%20PDFs/KAS-700-0146_PB.pdf.

[27] Bosch Sensortec GmbH. *BMP390 Datasheet, Document Number BST□BMP390□DS002□07, Revision 1.7*. 2021. URL: https://www.bosch-sensortec.com/media/boschsensortec/downloads/datasheets/bst-bmp390-ds002.pdf.

[28] Salil Luesutthiviboon et al. “Aeroacoustic benchmarking of trailing-edge noise from NACA 63 3–018 airfoil with trailing-edge serrations”. In: *AIAA Journal* 61.1 (2023), pp. 329–354.

[29] Delft University of Technology. *Propeller models*. https://www.tudelft.nl/en/ae/organisation/departments/flow-physics-and-technology/flight-performance-propulsion/flight-performance/propeller-aerodynamics/facilities/propeller-models. Faculty of Aerospace Engineering, Flow Physics and Technology; Flight Performance & Propulsion; Facilities. Accessed 2025-10-05.

[30] N Van Arnhem. “Unconventional Propeller- Airframe Integration for Transport Aircraft Configurations”. PhD thesis. Delft University of Technology, 2022.

[31] Markus Raffel et al. *Particle image velocimetry: a practical guide*. springer, 2018.

[32] Ehab Elsaadawy and Colin Britcher. “Experimental investigation of the effect of propeller slipstream on boundary layer behavior at low reynolds number”. In: *18th Applied Aerodynamics Conference*. 2000, p. 4123.

[33] B. Zang, Y. Mayer, and M. Azarpeyvand. “On the aerodynamic and aeroacoustic characteristics of a NACA 65-410 airfoil at moderate Reynolds number”. In: *AIAA AVIATION 2020 FORUM* (2020). DOI: 10.2514/6.2020-2599.

[34] Pradeep Singh et al. “Insights into the transition of separation bubble over a rough surface at varying angles of attack”. In: *Physics of Fluids* (2024). DOI: 10.1063/5.0190786.

[35] Changliang Ye et al. “Investigation on transition characteristics of laminar separation bubble on a hydrofoil”. In: *Physics of Fluids* (2023). DOI: 10.1063/5.0170024.

[36] SP Sparks and SJ Miley. *Development of a propeller afterbody analysis with contracting slipstream*. Tech. rep. SAE Technical Paper, 1983.

[37] Ahmed ELTaweel and Meng Wang. “Numerical Simulation of Broadband Noise from Airfoil-Wake Interaction”. In: *17th AIAA/CEAS Aeroacoustics Conference (32nd AIAA Aeroacoustics Conference)*. AIAA, 2011. DOI: 10.2514/6.2011-2802. eprint: https://arc.aiaa.org/doi/pdf/10.2514/6.2011-2802. URL: https://arc.aiaa.org/doi/abs/10.2514/6.2011-2802.

[38] Adrian Grille Guerra et al. “Experimental characterization of an unsteady laminar separation bubble on a pitching wing”. In: *Experiments in Fluids* 64.1 (2023), p. 16.

[39] M. Breuer. “Effect of Inflow Turbulence on an Airfoil Flow with Laminar Separation Bubble: An LES Study”. In: *Flow, Turbulence and Combustion* 101 (2018), pp. 433–456. DOI: 10.1007/s10494-017-9890-2.

[40] Dhanush Vittal-Shenoy et al. “Angle-of-attack and Mach number effects on the aeroacoustics of an SD7003 airfoil at Reynolds number 60,000”. In: *International Journal of Aeroacoustics* 22 (2023), pp. 131–152. DOI: 10.1177/1475472x221150173.

[41] Nur Syafiqah Jamaluddin et al. “Experimental analysis of a propeller noise in turbulent flow”. In: *Physics of Fluids* 35.7 (July 2023), p. 075106. DOI: 10.1063/5.0153326. URL: https://doi.org/10.1063/5.0153326.